Polymerization of Olefins through Heterogeneous Catalysis X: Modeling of Particle Growth and Morphology

R. A. HUTCHINSON, C. M. CHEN, and W. H. RAY*

Department of Chemical Engineering, University of Wisconsin–Madison, Madison, Wisconsin 53706

SYNOPSIS

The development of a detailed model describing particle growth in olefin copolymerization systems is presented. The Multigrain Model considers in detail monomer sorption, mass transfer, and changing porosity within the growing particle, as well as heat and mass transfer across the external film of the particle. The model predicts catalyst performance, including polymerization rates and particle morphology, in different reactor media without parameter adjustment. Internal void fractions are calculated through an examination of the relative growth rates within the growing particle. The model is used to examine the effects of mass transfer limitations, prepolymerization, and nonuniform metal distribution on the particle growth process. Model predictions of morphology show the same trends as observed experimentally.

INTRODUCTION

In spite of extensive research over many years, there is still a lack of understanding about several aspects of the process of heterogeneous catalyzed olefin polymerization, ranging from the kinetic mechanisms of active site initiation and deactivation, to the crystallization and morphology of the growing polymer particles and the removal of the heat of polymerization from the growing particle. These unresolved issues have made it difficult to systematically develop new catalysts and polymer products, with developments often requiring trial and error methods. Thus, a better fundamental understanding of the polymerization process can lead to a more systematic procedure of catalyst design, reactor optimization, and control.

Ray[1] suggests that there are three scales of interest for the modelling of transition metal catalyzed olefin polymerization. The macroscale level concerns reactor phenomena, such as heat removal, residence time distributions, and particle size distributions; these factors influence process control and product transitions in the reactor. Understanding the kinetics on a microscale level is important when discussing the effects of multiple types of active sites on MWD and copolymer composition; the mechanisms of site activation, polymer growth and crystallization, and catalyst deactivation occur at this scale. The mesoscale concerns phenomena between these two extremes—catalyst fragmentation, particle growth, and intraparticle and interparticle mass and heat transfer processes. This is the level upon which this article concentrates. Through a better understanding of the phenomena associated with particle growth, important insights in the areas of particle morphology, copolymer composition, and reactor scale-up are gained.

A typical solid catalyst used for olefin polymerization consists of porous particles of mean diameter 5–100 μm ("macroparticles"). Each catalyst macroparticle is an agglomeration of smaller fragments ("microparticles") of dimension 0.001–0.5 μm, the size dependent on catalyst preparation. It is on the surface of these catalyst fragments that the polymerization reaction occurs. During the reaction, the large pores in the catalyst macroparticle quickly fill up with the solid polymer and the catalyst undergoes breakup, as illustrated schematically in Figure 1(a).[2] Despite the spreading apart of the catalyst fragments, the corresponding polymer microparticles remain loosely associated to one another within the

* To whom correspondence should be addressed.

Journal of Applied Polymer Science, Vol. 44, 1389–1414 (1992)
 CCC 0021-8995/92/081389-26$04.00

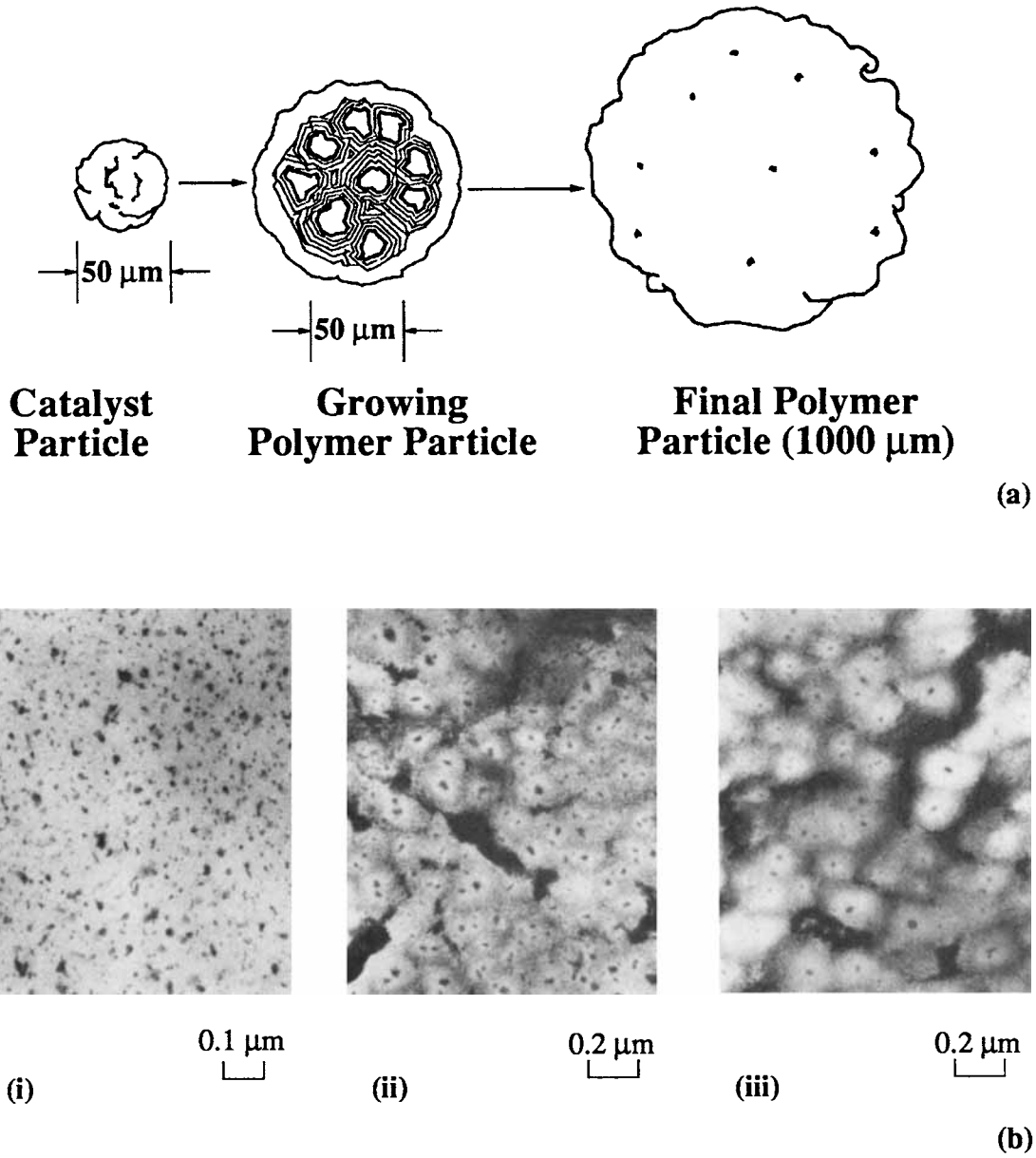

Figure 1 Polyolefin particle growth: (a) Schematic representation (taken from Ref. 2); (B) TEM micrographs of polypropylene particle at yields of: (i) 12 g/g-cat, (ii) 108 g/g-cat, (iii) 880 g/g-cat (taken from Ref. 3).

growing macroparticle. In general, replication is observed; there is a one-to-one correspondence between catalyst and polymer, both at the microparticle and macroparticle levels. By the end of polymerization, the polymer particle has increased from its original catalyst particle size to a final size on the order of 1 mm, and catalyst residues are measured in parts per million. Figure 1 (b) shows transmission electron micrographs of propylene polymerization at various stages of growth over a $TiCl_3$ catalyst.[3] At the later stages of polymerization, distinct polymer microparticles are observed, each containing a single catalyst fragment.

A detailed model of particle growth, based on the description presented above, has been developed by Floyd et al.[4-7] Earlier modelling concepts, most notably those of Begley,[8] Singh and Merrill,[9] and Schmeal and Street,[10] were refined by Nagel, Kirillov, and Ray[11] to form the structural basis for our model. The Multigrain Model (MGM) of Floyd et

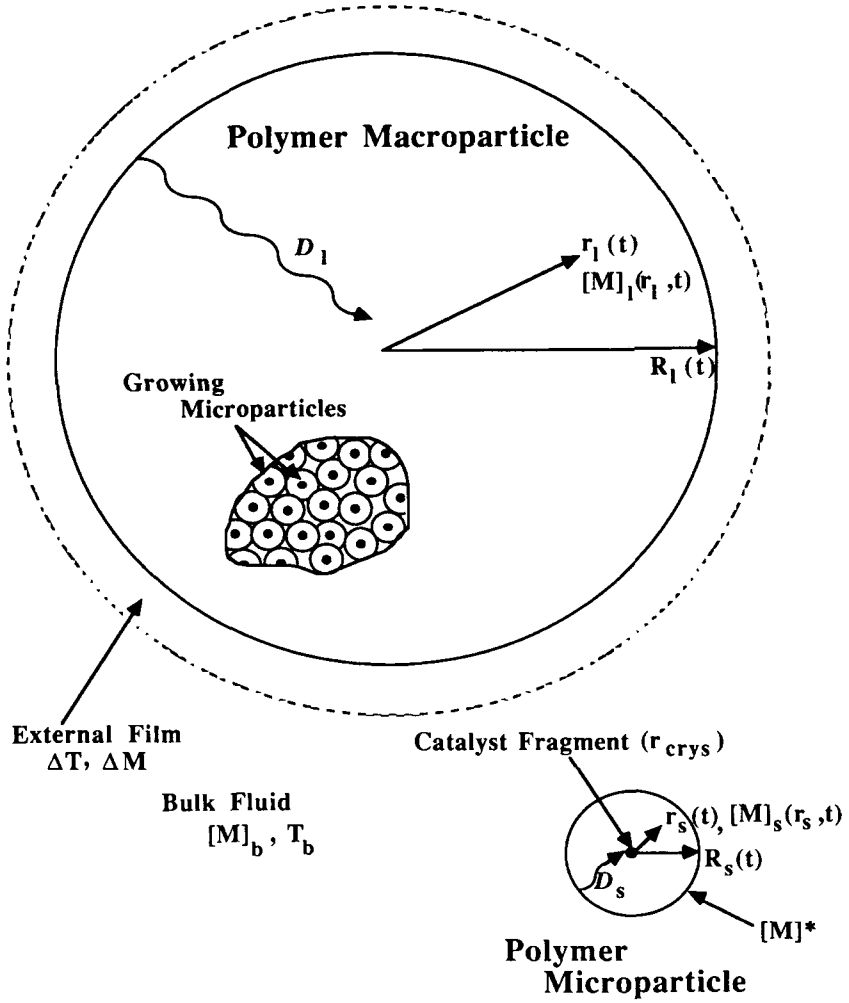

Figure 2 The multigrain model of particle growth.

al., shown schematically in Figure 2, considers transport phenomena within the particle at two distinct levels. Both large scale diffusion (subscript "ℓ") through the macroparticle, and microparticle diffusion (subscript "s") through the polymer film surrounding the catalyst fragments are considered. External boundary layer gradients (temperature and concentration) are also included in this model.

The MGM was developed in an attempt to account for the broad molecular weight distribution (MWD) characteristic of heterogeneous catalyzed olefin polymerizations.[11] Floyd et al.[7] found that, with reasonable estimates for diffusivities and other parameters, transport effects are not enough to account for the observed broad distributions; differences in site activities caused by the heterogeneous nature of the catalyst must also be considered. Intraparticle diffusion limitations affect the shape of the observed rate curves and the observed activation energies more strongly than the polymer properties. The degree of diffusion resistance is strongly dependent on the initial catalyst size and structure. The dynamic modelling done by Chiovetta et al.[12-14] closely parallels the work of Floyd et al. and draws many of the same conclusions. Their modelling concentrates on the morphological growth of the particle, especially catalyst breakup, and does not contain the kinetic complexities of the model of Floyd et al.

In this article, an improved version of the MGM is presented. The goal of the modifications are threefold: to extend the model to detailed copolymerization kinetics; to generalize the representation so that the model will be useful for predictive scale-up between different reactor systems; and to extend the model so that it will have some predictive capabilities for particle morphology.

MODELLING OF PARTICLE GROWTH

The full set of material and energy balances for the growing polymer particle is presented in Table I. The equations differ from those presented by Floyd et al.[4-7] in notation only. In the derivation of these balances, the following assumptions are made:

- Replication is observed, both at the macro and microparticle level.
- Catalyst is completely ruptured at time zero.
- Particles (micro and macro) are of spherical shape.
- Polymer production occurs pseudo-homogeneously at the macroparticle scale.

Using reasonable estimates for important parameters, such as diffusivities and catalyst crystallite sizes, Floyd performed an informative bounding analysis to examine the importance of the various heat and mass transfer resistances. It was shown that concentration gradients may exist within the macro and microparticles, but temperature gradients are negligible. This conclusion has been supported by the modelling work of Laurence and Chiovetta[12] and Böhm et al.[15] Floyd also shows that use of the quasi steady state approximation (QSSA) is valid for the microparticle material balance. This analysis leads to the elimination of the intraparticle energy balances of Table I, and simplifies the microparticle mass balance to an algebraic equation. The remaining partial differential equation, the macroparticle mass balance, is solved by Floyd et al. using a predictor–corrector finite difference scheme.[6]

Material Balances

The material balances from Table I can be easily extended to copolymerization systems. For the polymer microparticle:

$$\frac{\partial[\mathrm{M}_i]_s}{\partial t} = \frac{1}{r_s^2}\frac{\partial}{\partial r_s}\left((D_i)_s r_s^2 \frac{\partial[\mathrm{M}_i]_s}{\partial r_s}\right) \qquad (1)$$

$$\text{B.C.} \quad r_s = \mathrm{R}_s: \qquad [\mathrm{M}_i]_s = \eta_i^* [\mathrm{M}_i]_\ell$$

Table I The Multigrain Model: Full Mass and Energy Balances

Macroparticle ($0 \le r_l \le \mathrm{R}_l$):

$$\frac{\partial[\mathrm{M}]_l}{\partial t} = \frac{1}{r_l^2}\frac{\partial}{\partial r_l}\left(D_l r_l^2 \frac{\partial[\mathrm{M}]_l}{\partial r_l}\right) - \mathrm{R}_v$$

$$\frac{\partial \mathrm{T}_l}{\partial t} = \frac{1}{r_l^2}\frac{\partial}{\partial r_l}\left(\left(\frac{k_e}{\rho_{\mathrm{pol}}\mathrm{C}_p}\right) r_l^2 \frac{\partial \mathrm{T}_l}{\partial r_l}\right) - \frac{(-\Delta \mathrm{H}_p)}{\rho_{\mathrm{pol}}\mathrm{C}_p}\mathrm{R}_v$$

B.C. $r_l = 0$: $\dfrac{\partial[\mathrm{M}]_l}{\partial r_l} = \dfrac{\partial \mathrm{T}_l}{\partial r_l} = 0$

$r_l = \mathrm{R}_l$: $D_l \dfrac{\partial[\mathrm{M}]_l}{\partial r_l} = k_s([\mathrm{M}]_b - [\mathrm{M}]_l); \quad k_e \dfrac{\partial \mathrm{T}_l}{\partial r_l} = h(\mathrm{T}_b - \mathrm{T}_l)$

I.C. $t = 0$: $[\mathrm{M}]_l = [\mathrm{M}]_0; \quad \mathrm{T}_l = \mathrm{T}_0; \quad \mathrm{R}_l = r_{\mathrm{cat}}$

Microparticle ($r_{\mathrm{crys}} \le r_s \le \mathrm{R}_s$):

$$\frac{\partial[\mathrm{M}]_s}{\partial t} = \frac{1}{r_s^2}\frac{\partial}{\partial r_s}\left(D_s r_s^2 \frac{\partial[\mathrm{M}]_s}{\partial r_s}\right)$$

$$\frac{\partial \mathrm{T}_s}{\partial t} = \frac{1}{r_s^2}\frac{\partial}{\partial r_s}\left(\left(\frac{k_e}{\rho_{\mathrm{pol}}\mathrm{C}_p}\right) r_s^2 \frac{\partial \mathrm{T}_s}{\partial r_s}\right)$$

B.C. $r_s = \mathrm{R}_s$: $[\mathrm{M}]_s = \eta^*[\mathrm{M}]_l; \quad \mathrm{T}_s = \mathrm{T}_l$

$r_s = r_{\mathrm{crys}}$: $(4\pi(r_{\mathrm{crys}})^2) D_s \dfrac{\partial[\mathrm{M}]_s}{\partial r_s} = \left(\dfrac{4\pi}{3}(r_{\mathrm{crys}})^3\right)\mathrm{R}_p;$

$$-(4\pi(r_{\mathrm{crys}})^2) k_e \frac{\partial \mathrm{T}_s}{\partial r_s} = \left(\frac{4\pi}{3}(r_{\mathrm{crys}})^3\right)(-\Delta \mathrm{H}_p)\mathrm{R}_p$$

I.C. $t = 0$: $[\mathrm{M}]_s = [\mathrm{M}]_0; \quad \mathrm{T}_s = \mathrm{T}_0; \quad \mathrm{R}_s = r_{\mathrm{crys}}$

$$r_s = r_{crys}: \quad (4\pi(r_{crys})^2)(D_i)_s \frac{\partial[M_i]_s}{\partial r_s} = \left(\frac{4\pi}{3}(r_{crys})^3\right)(R_p)_i$$

I.C. $t = 0$: $[M_i]_s = [M_i]_0$

$R_s = \phi_0 r_{crys}$

Nonmenclature is as depicted in Figure 2. The initial microparticle growth factor (ϕ_0) is unity for a particle with no prepolymerization. The expression for the consumption rate of monomer i in the microparticle, $(R_p)_i$, has units of (mol-i/cm^3-cat s) and is developed in the following section; η_i^* is the sorption factor, also defined later. Assuming the diffusivity of species i across the microparticle, $(D_i)_s$, is constant and employing the QSSA, this equation is integrated to give:

$$[M_i]_s = \eta_i^* [M_i]_\ell + \frac{(r_{crys})^3}{3(D_i)_s}(R_p)_i\left(\frac{1}{R_s} - \frac{1}{r_s}\right) \quad (2)$$

At the surface of the catalyst fragment ($r_s = r_{crys}$), the expression for monomer concentration is:

$$[M_i]_{crys} = \eta_i^* [M_i]_\ell - \frac{(r_{crys})^2}{3(D_i)_s}(R_p)_i\left(1.0 - \frac{1}{\phi}\right) \quad (3)$$

where ϕ, the microparticle growth factor, is defined as:

$$\phi = \frac{R_s}{r_{crys}} \quad (4)$$

Equation (3) indicates that as the microparticle grows in size, concentration gradients across the polymer layer increase. However, as shown by Floyd et al.[5] for homopolymerization systems, the degree of microparticle diffusion limitation rapidly approaches an asymptote and is nearly constant for growth factors larger than 10.

At the macroparticle level, the mass balance is:

$$\frac{\partial[M_i]_\ell}{\partial t} = \frac{1}{r_\ell^2}\frac{\partial}{\partial r_\ell}\left((D_i)_\ell r_\ell^2 \frac{\partial[M_i]_\ell}{\partial r_\ell}\right) - (R_v)_i \quad (5)$$

B.C. $r_\ell = 0$: $\dfrac{\partial[M_i]_\ell}{\partial r_\ell} = 0$

$$r_\ell = R_\ell: \quad (D_i)_\ell \frac{\partial[M_i]_\ell}{\partial r_l} = k_{s_i}([M_i]_b - [M_i]_\ell)$$

I.C. $t = 0$: $[M_i]_\ell = [M_i]_0$

$R_\ell = \phi_0 r_{cat}$

The external boundary condition takes into consideration boundary layer mass transfer limitations; the mass transfer coefficient is estimated as outlined in Ref. 4.

The macroparticle volumetric rate of consumption of monomer i, $(R_v)_i$, has units of (mol-i/cm^3-part s) and is related to the microparticle consumption rate according to the expression:

$$(R_v)_i = (R_p)_i\left(\frac{(1-\epsilon)}{\phi^3}\right) \quad (6)$$

where ϵ is the local macroparticle void fraction. This expression illustrates the dilution effect caused by polymer formation within the macroparticle. As the microparticles grow in size, the macroparticle volumetric rate of polymerization decreases. Thus the most severe macroparticle mass transfer limitations are early in the particle lifetime.

Microparticle growth factor is calculated from a mass balance of polymer produced at all active sites:

$$\phi^3 = 1.0 + \frac{[Me]M_n \sum_{k=1}^{N_{sites}} \mu_0^k}{\rho_{pol}} \quad (7)$$

M_n is the number average molecular weight of the polymer chains in the microparticle and μ_0^k is the total bulk polymer chains produced at active site type k, as defined in the following section.

In addition to the material balances presented above, an overall energy balance is performed on the particle. The balance across the external boundary layer is:

$$(V\rho C_p)_{pol}\frac{dT_s}{dt} = (-\Delta H_p)(R_p)_{part}V_{cat} - [hA_p(T_s - T_b)] \quad (8)$$

In this equation the heat transfer coefficient is estimated according to the correlations presented in Ref. 4. The total rate of polymer production in the particle, $(R_p)_{part}$, is calculated according to:

$$(R_p)_{part} = \frac{\int_V \sum_{i=1}^{N_{mon}} (R_p)_i dV}{\int_V dV} \quad (9)$$

Numerical Solution Technique

Floyd et al.[6] employed a finite difference scheme to solve for monomer concentrations as a function of time and space. With the introduction of multiple monomers and a more comprehensive kinetic scheme to the model, the solution technique has been extensively modified.[16]

Finite differences are still used to estimate the macroparticle concentration profiles as a function of radius. The discretization leads to a set of ordinary differential equations for macroparticle monomer concentrations, one for each grid point in space. The complete set of discretized macroparticle mass balances and corresponding sets of microparticle mass balances and moment equations are sent to a differential–algebraic system equation solver called DDASSL, developed and described by Petzold.[17] A more detailed step-by-step description of the solution technique follows. The description is for the case of constant void fraction; variable void fraction is discussed later in this section.

Grid Initialization

As shown in Figure 3, particle radius is discretized into N_s radial shells at time zero. The catalyst volume, thickness, and radial position of each shell are computed. Radius and catalyst volume are scaled so that:

$$r_{N_s} = 1.0 \tag{10}$$

$$\sum_{n=1}^{N_s} V_{n_0} = 1.0 - \epsilon_0 \tag{11}$$

Shells of equal radius or equal volume can be specified for the initialization.

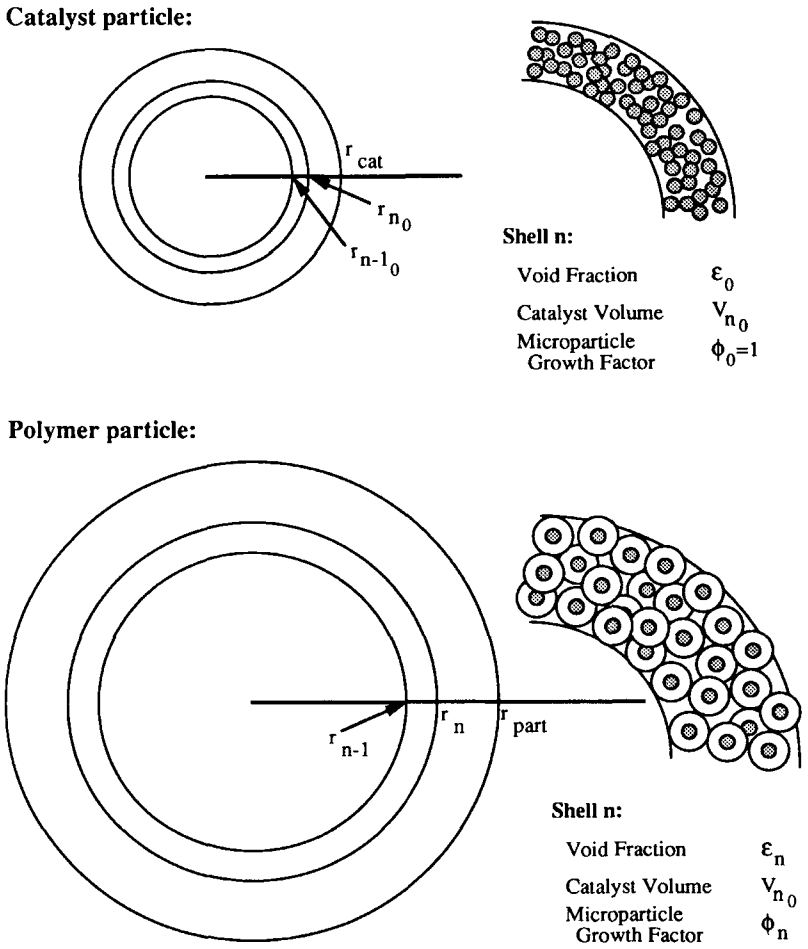

Figure 3 Schematic of discretization and tracking of particle growth in the MGM.

Discretization

The radial concentration term of eq. (5) is expanded, assuming constant $(D_i)_e$, as follows:

$$(D_i)_e\left(\frac{2}{r_n}\left.\frac{\partial[\mathrm{M}_i]}{\partial r}\right|_n + \left.\frac{\partial^2[\mathrm{M}_i]}{\partial r^2}\right|_n\right) \tag{12}$$

The first and second derivative terms are approximated with the discretization scheme presented in Ref. 16—central differences on an uneven grid derived using Taylor series expansions. Boundary conditions are approximated using one-sided differences.

Grid Update

The amount of catalyst in each shell is kept constant with time. As DDASSL sends back new estimates of concentrations and microparticles growth factors, it is necessary to update the grid positions. Note that shells at different positions along the particle radius will be growing at different rates. If constant void fraction throughout the growing particle is assumed, the position of grid point r_n is calculated from a volume balance over shell n:

$$\phi_n^3 \mathrm{V}_{n_0} = (1 - \epsilon)(r_n^3 - r_{n-1}^3) \tag{13}$$

With the variable time step employed by DDASSL, changes with time can be tracked both accurately and efficiently. A very small time step is necessary to track the rapid change in particle size at early time; later in the particle lifetime much larger steps are taken without loss of accuracy.

Modelling of Variable Void Fraction

It is observed experimentally that polymer of low bulk density is often produced at high rates of polymerization, but adding a prepolymerization step can result in significantly higher bulk densities.[18] It is hypothesized that poor particle morphology is a result of high intraparticle void fractions resulting from uneven rates of growth within the polymer macroparticle. In order to examine the effect of uneven growth rates on particle morphology, the assumption of constant void fraction within the macroparticle, implemented by Floyd et al.,[5-7] must be relaxed.

With variable void fraction, the expansion of the radial concentration term in eq. (5) must be modified. Diffusivity within the macroparticle is assumed to be proportional to void fraction according to the expression:

$$(D_i)_e = \frac{\epsilon(D_i)_b}{\tau} \tag{14}$$

Thus the expansion of the radial gradient becomes:

$$\frac{(D_i)_b}{\tau}\left(\frac{2\epsilon_n}{r_n}\left.\frac{\partial[\mathrm{M}_i]}{\partial r}\right|_n + \epsilon_n\left.\frac{\partial^2[\mathrm{M}_i]}{\partial r^2}\right|_n + \left.\frac{\partial\epsilon}{\partial r}\right|_n\left.\frac{\partial[\mathrm{M}_i]}{\partial r}\right|_n\right) \tag{15}$$

For variable void fraction, the term $\partial\epsilon/\partial r$ is approximated using finite differences. For constant void fraction, $\partial\epsilon/\partial r$ is zero and the expression collapses to eq. (12).

The assumption of constant void fraction is also used in the volume balance (eq. 13), which tracks the position of the radial grid points. The position of r_n is calculated from known values of r_{n-1}, ϕ_n^3, and ϵ. Equation (13) is still valid when the assumption of constant void fraction is relaxed; however, the equation now contains two unknowns, r_n and the local void fraction, ϵ_n:

$$\phi_n^3 \mathrm{V}_{n_0} = (1 - \epsilon_n)(r_n^3 - r_{n-1}^3) \tag{16}$$

A new equation must be introduced to solve for the additional unknown.

In physical terms, the case of constant void fraction is equivalent to assuming that polymer microparticles, within the macroparticle, rearrange themselves in order to keep the void fraction constant, independent of their relative growth rates. This neglects the forces exerted on each microparticle by its immediate neighbors. A more valid assumption is that the spatial arrangement of microparticles within the growing particle does not change; outward shell movement is a result of the pressures exerted by the growing microparticles within that shell. Thus if the microparticles in the interior layers of the particle do not grow at a rate sufficient to keep up with those in shell n, an increase in internal void fraction occurs. If microparticles in the interior shells grow at the same rate as those in shell n, the void fraction within the shell remains constant at its original value, ϵ_0. Shell position is only dependent on original shell position, r_{n_0}, and the local growth factor of microparticles within the shell:

$$r_n = r_{n_0}\phi_n \tag{17}$$

Values of r_n and r_{n-1} are used in eq. (16) to calculate ϵ_n, the local void fraction. Note that the void fraction at the center of the particle remains constant at the initial particle void fraction, ϵ_0. Other shells have a void fraction greater than or equal to this value.

Representation of Active Metal Profiles

Ziegler–Natta catalysts are often prepared by contacting a support particle with liquid active metal salts such as $TiCl_4$. Under some preparation conditions, it is possible that less of the active metal reaches the interior of the particle compared with the outer edges. This uneven metal concentration can cause uneven growth rates within the macroparticle, affecting final particle morphology. In order to model this effect, an enhancement has been added to the model, which allows metal concentration profiles to be specified as a function of radius. This is accomplished by assuming that the weight fraction metal (g − Me/g-cat) can be represented by the following function in terms of dimensionless radial position:

$$w_{me} = a + br + cr^2 + d\exp(fr) \qquad (18)$$

The average metal fraction between the center of the particle and position r_n is obtained by integrating over the particle volume:

$$\bar{w}_{me}|_0^{r_n} = \frac{\int_0^{r_n} w_{me} dV}{\int_0^{r_n} dV} \qquad (19)$$

For shell n between radial grid points n and $n-1$, the metal fraction is given by:

$$(w_{me})_n = \frac{\bar{w}_{me}|_0^{r_n} r_n^3 - \bar{w}_{me}|_0^{r_{n-1}} r_{n-1}^3}{r_n^3 - r_{n-1}^3} \qquad (20)$$

Local metal concentration in the shell is calculated from weight fractions according to:

$$[\mathrm{Me}]_n = \frac{(w_{me})_n \rho_{\mathrm{cat}}}{\mathrm{MW}_{me}} \qquad (21)$$

The effect of uneven metal distribution within the particle is examined in the examples at the end of the article.

MODELLING OF KINETICS AND CHAIN GROWTH

Radial gradients in the growing polymer particle, either of active metal or of monomers, create a distributed system in which the local rates of monomer incorporation and chain growth are position dependent. By including a complete kinetic scheme for copolymerization in the model, it is possible to predict polymer composition and molecular weights in the growing particle as a function of position and time. This section outlines the development of such a model. In the development below, the monomer concentration, denoted by $[M_i]$, is equivalent to the monomer concentration at the surface of the catalyst fragments presented in eq. (3), $[M_i]_{\mathrm{crys}}$; the nomenclature has been changed for the sake of brevity.

Kinetic Scheme and Active Sites Balances

A complete kinetic representation of catalyzed olefin polymerization has been developed by Chen[19] for a multiple monomer, multiple site system. As summarized in Table II, each active site type (superscript k) has a complete kinetic scheme involving activation, deactivation, site transformation, and chain transfer reactions. The reactions can take place spontaneously, or involve cocatalyst, hydrogen, monomer, electron donor, or poison. The concentration of active sites is expressed on a fractional basis, normalized by the total amount of active metal in the catalyst; the following quantities have units of (mol/mol-Me):

- C_∞, maximum fraction of metal that can form active sites;
- C_p, potential sites not yet activated;
- C_d, deactivated sites;
- P_*^k, active sites of type k (vacant and occupied by growing chain);
- P_0^k, vacant active sites of type k;
- $P_{n,i}^k$, growing polymer chain of length n ending with monomer i, at active site type k;
- D_n^k, dead polymer chain of length n produced at active site type k;
- λ_{0i}^k, total growing polymer chains ending with monomer i at active site type k;
- μ_0^k, total bulk (living and dead) polymer chains produced at site type k.

The nomenclature for rate coefficients and reaction orders are defined by Table II. Note that if a growing chain is attached to the active site, a dead polymer chain will be formed during deactivation and trans-

Table II Kinetic Scheme for Catalyzed Olefin Polymerization

Reaction		Rate Constant	Reaction Order
Activation:			
Spontaneous:	$C_p \rightarrow P_0^k$	$k_{a\mathrm{Sp}}^k$	$\gamma_{a\mathrm{Sp}}^k$
by Aluminum Alkyl (A):	$C_p + [A] \rightarrow P_0^k$	$k_{a\mathrm{A}}^k$	$\gamma_{a\mathrm{A}}^k$
by Electron Donor (E):	$C_p + [E] \rightarrow P_0^k$	$k_{a\mathrm{E}}^k$	$\gamma_{a\mathrm{E}}^k$
by Hydrogen (H_2):	$C_p + [H_2] \rightarrow P_0^k$	$k_{a\mathrm{H}}^k$	$\gamma_{a\mathrm{H}}^k$
by Monomer (M_i):	$C_p + M_i \rightarrow P_0^k + M_i$	$k_{a\mathrm{Mi}}^k$	1
Deactivation:			
Spontaneous:	$P_*^k \rightarrow C_d(+D_n^k)$	$k_{d\mathrm{Sp}}^k$	$\gamma_{d\mathrm{Sp}}^k$
by Poison (Z):	$P_*^k + [Z] \rightarrow C_d(+D_n^k)$	$k_{d\mathrm{Z}}^k$	$\gamma_{d\mathrm{Z}}^k$
by Aluminum Alkyl (A):	$P_*^k + [A] \rightarrow C_d(+D_n^k)$	$k_{d\mathrm{A}}^k$	$\gamma_{d\mathrm{A}}^k$
by Electron Donor (E):	$P_*^k + [E] \rightarrow C_d(+D_n^k)$	$k_{d\mathrm{E}}^k$	$\gamma_{d\mathrm{E}}^k$
by Hydrogen (H_2):	$P_*^k + [H_2] \rightarrow C_d(+D_n^k)$	$k_{d\mathrm{H}}^k$	$\gamma_{d\mathrm{H}}^k$
by Monomer (M_i):	$P_*^k + M_i \rightarrow C_d(+D_n^k)$	$k_{d\mathrm{Mi}}^k$	1
Transformation:			
Spontaneous:	$P_*^{k_1} \rightarrow P_0^{k_2}(+D_n^{k_1})$	$k_{\mathrm{stSp}}^{k_1 k_2}$	1
by Poison (Z):	$P_*^{k_1} + [Z] \rightarrow P_0^{k_2}(+D_n^{k_1})$	$k_{\mathrm{stZ}}^{k_1 k_2}$	$\gamma_{\mathrm{stZ}}^{k_1 k_2}$
by Aluminum Alkyl (A):	$P_*^{k_1} + [A] \rightarrow P_0^{k_2}(+D_n^{k_1})$	$k_{\mathrm{stA}}^{k_1 k_2}$	$\gamma_{\mathrm{stA}}^{k_1 k_2}$
by Electron Donor (E):	$P_*^{k_1} + [E] \rightarrow P_0^{k_2}(+D_n^{k_1})$	$k_{\mathrm{stE}}^{k_1 k_2}$	$\gamma_{\mathrm{stE}}^{k_1 k_2}$
by Hydrogen (H_2):	$P_*^{k_1} + [H_2] \rightarrow P_0^{k_2}(+D_n^{k_1})$	$k_{\mathrm{stH}}^{k_1 k_2}$	$\gamma_{\mathrm{stH}}^{k_1 k_2}$
Chain Transfer:			
Spontaneous:	$P_{n,i}^k \rightarrow P_0^k + D_n^k$	$k_{t\mathrm{Spi}}^k$	1
to Aluminum Alkyl (A):	$P_{n,i}^k + [A] \rightarrow P_0^k + D_n^k$	$k_{t\mathrm{Ai}}^k$	$\gamma_{t\mathrm{Ai}}^k$
to Electron Donor (E):	$P_{n,i}^k + [E] \rightarrow P_0^k + D_n^k$	$k_{t\mathrm{Ei}}^k$	$\gamma_{t\mathrm{Ei}}^k$
to Hydrogen (H_2):	$P_{n,i}^k + [H_2] \rightarrow P_0^k + D_n^k$	$k_{t\mathrm{Hi}}^k$	$\gamma_{t\mathrm{Hi}}^k$
to Monomer (M_j):	$P_{n,i}^k + M_j \rightarrow P_{1,j}^k + D_n^k$	$k_{t\mathrm{M}ij}^k$	1
Propagation:			
First monomer unit: (Initiation)	$P_0^k + M_i \rightarrow P_{1,i}^k$	k_{0i}^k	1
Additional units: (Propagation)	$P_{n,i}^k + M_j \rightarrow P_{n+1,j}^k$	k_{pij}^k	1

formation reactions. Also, chain transfer to monomer leads to the formation of a live polymer chain of length unity; chain transfer to all other species results in a vacant active site.

With these definitions, site balance equations are written as:

$$C_p = C_\infty - C_d - \sum_{k=1}^{N_{\mathrm{sites}}} P_*^k \tag{22}$$

$$P_0^k = P_*^k - \sum_{i=1}^{N_{\mathrm{mon}}} \lambda_{0i}^k \tag{23}$$

C_∞ is an intrinsic quality of the catalyst; the other quantities depend on the importance of various activation, deactivation, transformation, and chain transfer reactions.

At this point in the development, the definition of lumped rate terms simplifies the notation used in the equations. For site activation we define:

$$\beta_a^k \equiv k_{a\mathrm{Sp}}^k C_p^{(\gamma_{a\mathrm{Sp}}^k - 1)} + k_{a\mathrm{A}}^k [A]^{\gamma_{a\mathrm{A}}^k} + k_{a\mathrm{E}}^k [E]^{\gamma_{a\mathrm{E}}^k} + k_{a\mathrm{H}}^k [H_2]^{\gamma_{a\mathrm{H}}^k} + \sum_{i=1}^{N_{\mathrm{mon}}} (k_{a\mathrm{Mi}}^k [M_i]) \tag{24}$$

Thus, the rate of activation of sites of type k is given by $\beta_a^k C_p$. Similarly, for site deactivation we define:

$$\beta_d^k \equiv k_{d\mathrm{Sp}}^k (\mathrm{P}_*^k)^{(\gamma_{d\mathrm{Sp}}^k - 1)} + k_{d\mathrm{Z}}^k [\mathrm{Z}]^{\gamma_{d\mathrm{Z}}^k} + k_{d\mathrm{A}}^k [\mathrm{A}]^{\gamma_{d\mathrm{A}}^k} + k_{d\mathrm{E}}^k [\mathrm{E}]^{\gamma_{d\mathrm{E}}^k} + k_{d\mathrm{H}}^k [\mathrm{H}_2]^{\gamma_{d\mathrm{H}}^k} + \sum_{i=1}^{\mathrm{N_{mon}}} (k_{d\mathrm{M}i}^k [\mathrm{M}_i]) \quad (25)$$

The rate of deactivation of sites of type k is given by $\beta_d^k \mathrm{P}_*^k$. Note that the reaction order of spontaneous deactivation is defined with respect to P_*^k, all active sites of type k. For transfer to a polymer chain ending in monomer i at site k, the following lumped parameter is defined:

$$\beta_{ti}^k \equiv k_{t\mathrm{Sp}i}^k + k_{t\mathrm{A}i}^k [\mathrm{A}]^{\gamma_{t\mathrm{A}i}^k} + k_{t\mathrm{E}i}^k [\mathrm{E}]^{\gamma_{t\mathrm{E}i}^k} + k_{t\mathrm{H}i}^k [\mathrm{H}_2]^{\gamma_{t\mathrm{H}i}^k} + \sum_{j=1}^{\mathrm{N_{mon}}} (k_{t\mathrm{M}ij}^k [\mathrm{M}_j]) \quad (26)$$

For the transformation of sites from type k_1 to k_2, we define:

$$\beta_{st}^{k_1 k_2} \equiv k_{st\mathrm{Sp}}^{k_1 k_2} + k_{st\mathrm{Z}}^{k_1 k_2} [\mathrm{Z}]^{\gamma_{st\mathrm{Z}}^{k_1 k_2}} + k_{st\mathrm{A}}^{k_1 k_2} [\mathrm{A}]^{\gamma_{st\mathrm{A}}^{k_1 k_2}} + k_{st\mathrm{E}}^{k_1 k_2} [\mathrm{E}]^{\gamma_{st\mathrm{E}}^{k_1 k_2}} + k_{st\mathrm{H}}^{k_1 k_2} [\mathrm{H}_2]^{\gamma_{st\mathrm{H}}^{k_1 k_2}} \quad (27)$$

The total rate of transformation of sites of type k_1 is the difference between the rate of generation by transformation and the rate of consumption by transformation and can be written as:

$$\sum_{k_2=1 \neq k_1}^{\mathrm{N_{sites}}} \beta_{st}^{k_2 k_1} \mathrm{P}_*^{k_2} - \sum_{k_2=1 \neq k_1}^{\mathrm{N_{sites}}} \beta_{st}^{k_1 k_2} \mathrm{P}_*^{k_1} \quad (28)$$

Note that transformation of site type k_1 to k_1 is not allowed because it is the same as chain transfer.

With these definitions of lumped rate terms, the remaining site balances are written as:

$$\frac{d\mathrm{P}_*^k}{dt} = \beta_a^k C_p - \beta_d^k \mathrm{P}_*^k + \sum_{k_1=1 \neq k}^{\mathrm{N_{sites}}} \beta_{st}^{k_1 k} \mathrm{P}_*^{k_1} - \sum_{k_1=1 \neq k}^{\mathrm{N_{sites}}} \beta_{st}^{k k_1} \mathrm{P}_*^k \quad (29)$$

$$\frac{dC_d}{dt} = \sum_{k=1}^{\mathrm{N_{sites}}} \beta_d^k \mathrm{P}_*^k \quad (30)$$

The rate of consumption (per cm^3 of catalyst) of monomer i by reaction is represented by:

$$(\mathrm{R}_p)_i = -[\mathrm{Me}] \left(\frac{d[\mathrm{M}_i]}{dt} \right)_{\mathrm{rxn}} = [\mathrm{Me}][\mathrm{M}_i] \sum_{k=1}^{\mathrm{N_{sites}}} \left[k_{d\mathrm{M}i}^k \mathrm{P}_*^k + k_{0i}^k \mathrm{P}_0^k + \sum_{j=1}^{\mathrm{N_{mon}}} (k_{t\mathrm{M}ji}^k + k_{pji}^k) \lambda_{0j}^k \right] \quad (31)$$

[Me] is the concentration of metal in the catalyst (mol-Me/cm^3-cat) defined in eq. (21). The dominant term in eq. (31) is that involving propagation.

Species Balances and Moment Equations

The balance on live (growing) polymer of chain length n (for $n = 1$ to ∞), ending with monomer i, at active site of type k, is written as:

$$\frac{d\mathrm{P}_{n,i}^k}{dt} = -\beta_d^k \mathrm{P}_{n,i}^k - \sum_{k_1=1 \neq k}^{\mathrm{N_{sites}}} \beta_{st}^{k k_1} \mathrm{P}_{n,i}^k - \beta_{ti}^k \mathrm{P}_{n,i}^k + \delta(n) \sum_{j=1}^{\mathrm{N_{mon}}} k_{t\mathrm{M}ji}^k \lambda_{0j}^k [\mathrm{M}_i] + \delta(n) k_{0i}^k \mathrm{P}_0^k [\mathrm{M}_i] + [1 - \delta(n)] \sum_{j=1}^{\mathrm{N_{mon}}} k_{pji}^k \mathrm{P}_{n-1,j}^k [\mathrm{M}_i] - \sum_{j=1}^{\mathrm{N_{mon}}} k_{pij}^k \mathrm{P}_{n,i}^k [\mathrm{M}_j] \quad (32)$$

where

$$\delta(j) = \begin{cases} 1 & \text{for } j = 1 \\ 0 & \text{for } j \neq 1 \end{cases} \quad (33)$$

The primary interest of this study is average polymer properties (i.e., rather than full molecular weight distributions); thus the method of moments is employed. The ℓ^{th} moment of live (growing) polymer ending with monomer i, at active site of type k, is a weighted sum of polymer chain concentrations and is defined as:

$$\lambda_{\ell i}^k \equiv \sum_{n=1}^{\infty} n^\ell \mathrm{P}_{n,i}^k \quad (34)$$

Equation (34) is applied to the live polymer balance (eq. 32); after working through the algebra, the live moment equation is derived:

$$\frac{d\lambda_{\ell i}^k}{dt} = [M_i]\left[\sum_{j=1}^{N_{mon}} k_{tMji}^k \lambda_{0j}^k + k_{0i}^k P_0^k\right] - \lambda_{\ell i}^k\left[\beta_d^k + \sum_{k_1=1\neq k}^{N_{sites}} \beta_{st}^{kk_1} + \beta_{ti}^k + \sum_{j=1}^{N_{mon}} k_{pij}^k [M_j]\right] + [M_i]\sum_{j=1}^{N_{mon}} k_{pji}^k\left[\sum_{q=0}^{\ell}\binom{\ell}{q}\lambda_{qj}^k\right] \quad (35)$$

where the binomial coefficient is given by:

$$\binom{\ell}{q} = \frac{\ell!}{q!(\ell-q)!} \quad (36)$$

For most heterogeneous Ziegler–Natta olefin polymerization systems for which chain lifetimes are short (and thus the dynamics of the polymer species fast), the QSSA can be applied to the live moment equations. As shown by Chen,[19] this results in a set of linear algebraic equations for λ_{0i}^k, λ_{1i}^k and λ_{2i}^k.

Bulk polymer is defined as consisting of both live (growing) and dead polymer. Thus a balance on bulk polymer of chain length n (for $n = 1$ to ∞) produced at active sites of type k can be written as:

$$\frac{d}{dt}\left(D_n^k + \sum_{i=1}^{N_{mon}} P_{n,i}^k\right) = \delta(n)\sum_{i=1}^{N_{mon}}\sum_{j=1}^{N_{mon}} k_{tMij}^k \lambda_{0i}^k [M_j] + \delta(n)\sum_{i=1}^{N_{mon}} k_{0i}^k P_0^k [M_i] + [1-\delta(n)]\sum_{i=1}^{N_{mon}}\sum_{j=1}^{N_{mon}} k_{pij}^k P_{n-1,i}^k [M_j] - \sum_{i=1}^{N_{mon}}\sum_{j=1}^{N_{mon}} k_{pij}^k P_{n,i}^k [M_j] \quad (37)$$

where $\delta(n)$ is defined by eq. (33). As for the live polymer balance, the method of moments is also applied to the bulk polymer balance. The ℓ^{th} moment of bulk polymer produced at active site of type k is defined as:

$$\mu_\ell^k \equiv \sum_{i=1}^{N_{mon}} \lambda_{\ell i}^k + \sum_{n=1}^{\infty} n^\ell D_n^k \quad (38)$$

After applying eq. (38) to the bulk polymer balance (eq. 37) and working through the algebra, the general bulk moment equation is derived:

$$\frac{d\mu_\ell^k}{dt} = \sum_{i=1}^{N_{mon}}\sum_{j=1}^{N_{mon}} k_{tMij}^k \lambda_{0i}^k [M_j] + P_0^k \sum_{i=1}^{N_{mon}} k_{0i}^k [M_i] + \sum_{i=1}^{N_{mon}}\sum_{j=1}^{N_{mon}} k_{pij}^k [M_j]\left[\sum_{q=0}^{\ell}\binom{\ell}{q}\lambda_{qi}^k - \lambda_{\ell i}^k\right] \quad (39)$$

By substituting $\ell = 0$, 1, and 2 into eq. (39), the balances for the zero, first, and second bulk polymer moments can be written as:

$$\frac{d\mu_0^k}{dt} = \sum_{i=1}^{N_{mon}}\sum_{j=1}^{N_{mon}} k_{tMij}^k \lambda_{0i}^k [M_j] + P_0^k \sum_{i=1}^{N_{mon}} k_{0i}^k [M_i] \quad (40)$$

$$\frac{d\mu_1^k}{dt} = \frac{d\mu_0^k}{dt} + \sum_{i=1}^{N_{mon}}\sum_{j=1}^{N_{mon}} k_{pij}^k [M_j]\lambda_{0i}^k \quad (41)$$

$$\frac{d\mu_2^k}{dt} = \frac{d\mu_0^k}{dt} + \sum_{i=1}^{N_{mon}}\sum_{j=1}^{N_{mon}} k_{pij}^k [M_j][\lambda_{0i}^k + 2\lambda_{1i}^k] \quad (42)$$

In physical terms, the first bulk polymer moment μ_1^k is equal to the total number of monomer units (for all monomer types, $i = 1$ to N_{mon}) incorporated into bulk polymer produced at active sites of type k. In order to model the composition of bulk (live + dead) copolymer, it is necessary to define an additional type of first moment:

$$\hat{\mu}_{1j}^k \equiv \sum_{m_j=1}^{\infty} (m_j) D_n^k + \sum_{m_j=1}^{\infty} (m_j) \sum_{i=1}^{N_{mon}} P_{n,i}^k \quad (43)$$

where m_j is the number of monomer j units incorporated into the polymer chain D_n^k or $P_{n,i}^k$. Thus, $\hat{\mu}_{1j}^k$ is the number of units of monomer j incorporated into bulk polymer produced at active sites of type k and may be calculated from:

$$\frac{d\hat{\mu}_{1j}^k}{dt} = -\left(\frac{d[M_j]}{dt}\right)_{rxn}^k - k_{dMj}^k P_*^k [M_j] \quad (44)$$

This development assumes that all reactions that consume monomer, except deactivation by monomer, lead to the incorporation of a monomer unit into the polymer chain. Note that:

$$\mu_1^k = \sum_{j=1}^{N_{mon}} \hat{\mu}_{1j}^k \quad (45)$$

Polymer Properties

Average polymer properties are calculated from the live and bulk polymer moments described above. The *compositions* of the copolymers are expressed in terms of a mole fraction of monomer i incorporated into the copolymer. The instantaneous composition of copolymer being produced at site k is calculated from the instantaneous rates of incorporation of the monomers into the polymer:

$$(\varphi_i)_{inst}^k = \frac{\frac{d\hat{\mu}_{1i}^k}{dt}}{\sum_{j=1}^{N_{mon}} \frac{d\hat{\mu}_{1j}^k}{dt}} \quad (46)$$

Under the QSSA, the instantaneous copolymer composition is equal to the live copolymer composition. The composition of the bulk copolymer produced at site k is given by:

$$(\varphi_i)^k_{\text{bulk}} = \frac{\hat{\mu}^k_{1i}}{\mu^k_1} \tag{47}$$

Composition of composite bulk polymer—the overall bulk polymer produced at all sites—is calculated according to:

$$(\varphi_i)_{\text{bulk}} = \frac{\sum_{k=1}^{N_{\text{sites}}} \hat{\mu}^k_{1i}}{\sum_{k=1}^{N_{\text{sites}}} \mu^k_1} \tag{48}$$

While composition of the copolymer is very important in determining many polymer properties, the ordering of the individual monomer units within the polymer chains is also important, especially in regard to copolymer crystallinity. One method of describing this ordering is through the *number average sequence lengths* of the individual monomers incorporated into the copolymer. The instantaneous probability of a live chain at site k with active end i adding another unit of monomer i is:

$$\text{Pr}^k_{ii} = \frac{k^k_{pii}[\text{M}_i]}{\beta^k_d + \sum_{k_1=1\neq k}^{N_{\text{sites}}} \beta^{kk_1}_{st} + \beta^k_{ti} + \sum_{j=1}^{N_{\text{mon}}} k^k_{pij}[\text{M}_j]} \tag{49}$$

As shown by Chen,[19] the instantaneous number average sequence length of monomer i in live polymer at active site k is given by:

$$\bar{N}^k_i = \frac{1}{1 - \text{Pr}^k_{ii}} \tag{50}$$

The instantaneous number average sequence length of monomer i in composite live polymer (at all sites) is given by:

$$\bar{N}_i = \frac{\sum_{k=1}^{N_{\text{sites}}} (\varphi_i)^k_{\text{inst}} \lambda^k_1}{\sum_{k=1}^{N_{\text{sites}}} (\varphi_i)^k_{\text{inst}} \lambda^k_1 / \bar{N}^k_i} \tag{51}$$

The *average chain lengths* of polymer are calculated from ratios of the polymer moments. For live (growing) polymer produced at site k, the number- and weight-average chain lengths (degrees of polymerization) are given by:

$$(\text{DP}_n)^k_{\text{live}} = \frac{\lambda^k_1}{\lambda^k_0} \quad (\text{DP}_w)^k_{\text{live}} = \frac{\lambda^k_2}{\lambda^k_1} \tag{52}$$

where

$$\lambda^k_\ell = \sum_{i=1}^{N_{\text{mon}}} \lambda^k_{\ell i} \tag{53}$$

In a similar fashion, the number- and weight-average chain lengths of bulk polymer produced at site k are calculated using:

$$(\text{DP}_n)^k_{\text{bulk}} = \frac{\mu^k_1}{\mu^k_0} \quad (\text{DP}_w)^k_{\text{bulk}} = \frac{\mu^k_2}{\mu^k_1} \tag{54}$$

The average chain lengths of composite bulk polymer are given by:

$$(\text{DP}_n)_{\text{bulk}} = \frac{\mu_1}{\mu_0} \quad (\text{DP}_w)_{\text{bulk}} = \frac{\mu_2}{\mu_1} \tag{55}$$

where

$$\mu_\ell = \sum_{k=1}^{N_{\text{sites}}} \mu^k_\ell \tag{56}$$

To relate average chain lengths to *average molecular weights* of the copolymers it is necessary to define an average molecular weight of the monomers (each having molecular weight MW_i) incorporated into the polymer for both live and bulk polymer at site k:

$$\overline{\text{MW}}^k_{\text{live}} \equiv \sum_{i=1}^{N_{\text{mon}}} (\varphi_i)^k_{\text{inst}} \text{MW}_i$$

$$\overline{\text{MW}}^k_{\text{bulk}} \equiv \sum_{i=1}^{N_{\text{mon}}} (\varphi_i)^k_{\text{bulk}} \text{MW}_i \tag{57}$$

With this value, number- and weight-average molecular weights and polydispersities of live and bulk polymer produced at site k are calculated according to:

$$(\text{M}_n)^k_{\text{live}} = \overline{\text{MW}}^k_{\text{live}} (\text{DP}_n)^k_{\text{live}}$$

$$(\text{M}_n)^k_{\text{bulk}} = \overline{\text{MW}}^k_{\text{bulk}} (\text{DP}_n)^k_{\text{bulk}} \tag{58}$$

$$(\text{M}_w)^k_{\text{live}} = \overline{\text{MW}}^k_{\text{live}} (\text{DP}_w)^k_{\text{live}}$$

$$(\text{M}_w)^k_{\text{bulk}} = \overline{\text{MW}}^k_{\text{bulk}} (\text{DP}_w)^k_{\text{bulk}} \tag{59}$$

$$Q^k_{\text{live}} = \frac{(M_w)^k_{\text{live}}}{(M_n)^k_{\text{live}}}\ ;\ Q^k_{\text{bulk}} = \frac{(M_w)^k_{\text{bulk}}}{(M_n)^k_{\text{bulk}}} \qquad (60)$$

Composite bulk polymer molecular weights (produced at all sites) are calculated in a similar fashion, using values of $(\varphi_i)_{\text{bulk}}$, $(DP_n)_{\text{bulk}}$ and $(DP_w)_{\text{bulk}}$. The weight fraction of bulk polymer produced at active sites of type k is calculated from:

$$w^k = \frac{\mu_0^k (M_n)^k_{\text{bulk}}}{\mu_0 (M_n)_{\text{bulk}}} \qquad (61)$$

Copolymer *crystallinity* and *density* are both strong functions of polymer composition—as comonomer content increases, polymer density and crystallinity decrease. In addition, polymers of identical composition, produced with different catalyst systems, may have different densities. This last observation is due to the heterogeneous nature of solid catalyst systems—polymer microstructure may vary from system to system or even from active site to active site. Due to these observations, an empirical approach is employed in estimating these values. Density of bulk polymer produced at site k is calculated according to:

$$\rho^k_{\text{pol}} = a + \sum_{i=2}^{N_{\text{mon}}} \{ b_i (\varphi_i)^k_{\text{bulk}} + c_i [(\varphi_i)^k_{\text{bulk}}]^2 + d_i [(\varphi_i)^k_{\text{bulk}}]^3 \} \qquad (62)$$

The value of "a" represents the homopolymer density for the principal monomer in the system; the other constants should be determined through the fit of experimental data. The relationship between crystallinity and density, assuming volume additivity between crystalline and amorphous polymer, is:

$$\alpha^k_v = \frac{\rho^k_{\text{pol},cr} - \rho^k_{\text{pol}}}{\rho^k_{\text{pol},cr} - \rho^k_{\text{pol},am}} \qquad (63)$$

where α^k_v is the amorphous volume fraction of the bulk polymer produced at site k. To use this expression, it is necessary to estimate densities as a function of polymer composition. Densities of 100% crystalline and amorphous polymer are estimated by a weighted sum of the homopolymer values:

$$\rho^k_{\text{pol},cr} = \sum_{i=1}^{N_{\text{mon}}} (\rho_{\text{pol},cr})_i (\varphi_i)^k_{\text{bulk}} \qquad (64)$$

$$\rho^k_{\text{pol},am} = \sum_{i=1}^{N_{\text{mon}}} (\rho_{\text{pol},am})_i (\varphi_i)^k_{\text{bulk}} \qquad (65)$$

The density and crystallinity of the composite bulk polymer (produced at all sites) is then determined by a weighted averaging of the densities and crystallinities of the polymer produced at each site type:

$$\frac{1}{\rho_{\text{pol}}} = \sum_{k=1}^{N_{\text{sites}}} \frac{w^k}{\rho^k_{\text{pol}}} \qquad (66)$$

$$\alpha_v = \rho_{\text{pol}} \sum_{k=1}^{N_{\text{sites}}} \frac{w^k \alpha^k_v}{\rho^k_{\text{pol}}} \qquad (67)$$

For the homopolymerization of α-olefins, the *tacticity* of the polymer is an important characteristic. The overall wt fraction of isotactic polymer produced at the active sites, I_{bulk}, can be calculated as a weighted average of the wt fraction of isotactic polymer produced at each active site, I^k_{bulk}:

$$I_{\text{bulk}} = \sum_{k=1}^{N_{\text{sites}}} w^k I^k_{\text{bulk}} \qquad (68)$$

ESTIMATION OF TRANSPORT PROPERTIES

In order to accurately represent catalyst performance under a range of operating conditions and systems, it is necessary that physical and transport properties be calculated as a function of operating conditions and system composition. The correlations summarized in this section are used in the implementation of the full multigrain particle model.

Fluid Physical Properties

The physical properties of the reactor fluid affect the particle growth in several ways. Fluid properties such as viscosity, thermal conductivity, heat capacity, and diffusivity are necessary in order to estimate heat and mass transfer coefficients between the particle and fluid. The diffusion coefficient is also used in the calculation of macroparticle diffusivity, as outlined below. The correlations used to estimate monomer concentrations and fluid properties as a function of system composition and operating conditions are discussed in Ref. 16. Gas phase, supersaturated liquid phase systems, and liquid systems at vapor–liquid equilibrium can all be considered.

Macroparticle Diffusivity

As suggested by Floyd et al.,[5] the diffusion of monomer through the macroparticle is similar to diffusion through a porous catalyst. Macroparticle diffusivity

for monomer i is related to the monomer diffusivity in the reactor fluid according to:

$$(D_i)_\ell = \frac{\epsilon(D_i)_b}{\tau} \tag{14}$$

where ϵ is the void fraction of the macroparticle and τ is a tortuosity factor. The tortuosity factor is usually in the range of 2–7; if nothing is known about the catalyst structure a value of 4 is recommended.[20]

Sorption Factors

The importance of monomer sorption effects on polymerization behavior are clearly illustrated in Ref. 21; the extent of monomer solubility in the polymer phase is very different in gas and liquid phase polymerization systems. The sorption coefficient affects the local concentration of monomer in the microparticle, as shown by eq. 3. In Ref. 21, Hutchinson and Ray also describe the problems in modelling the extent of sorption, and the shortage of data on sorption of liquids in polyolefins. In order to introduce a generalized correlation to predict the extent of sorption, some simplifications must be made. Thus, in the present version of the model, the following approximate relations are used.

For gas phase systems, Henry's Law is assumed for the sorption of monomer from the gas phase into the amorphous phase of a semicrystalline polyolefin. The correlation, suggested by Stern et al.,[22] is used to estimate the Henry's Law solubility coefficient (k_H^*, mol/cm^3-atm) for the monomers in amorphous polyolefin as a function of system temperature:

$$\log(k_H^*) = -5.38 + 1.08(T_c/T)^2 \tag{69}$$

T_c is the critical temperature of the sorbing component. Based on this estimate, a sorption factor for each monomer is estimated according to:

$$\eta_i^* = \frac{[M_i]^*}{[M_i]_b} = \frac{k_{H_i}^* P}{\hat{\rho}} \tag{70}$$

where P is the total reactor pressure (atm) and $\hat{\rho}$ is the molar density of the gas in the reactor. This correlation provides a reasonable estimate of sorption effects, but does not take into account enhanced sorption caused by deviations from Henry's Law behavior.

For liquid phase sorption, it is assumed that all components partition equally in the polymer phase:

$$\eta_i^* = \frac{[M_i]^*}{[M_i]_b} = 1.0 - v_{pol} \tag{71}$$

where v_{pol} is the volume fraction of polymer in the swollen amorphous polymer phase. The partition coefficient is empirically related to system temperature according to the quadratic fits of experimental data taken from Ref. 16 for the heptane-PP and hexane-PE systems:

$$v_{pol} = a + b(1/T) + c(1/T)^2 \tag{72}$$

heptane-PP: $a = -2.1820$,

$b = 1.4938\text{E}3$, $c = -1.9434\text{E}5$,

hexane-PE: $a = -3.6329$,

$b = 2.3547\text{E}3$, $c = -3.1243\text{E}5$.

Extrapolation to other systems or outside the temperature range of the experimental data is not recommended.

Microparticle Diffusivity

The microparticle diffusivity coefficient, $(D_i)_s$, is a measure of monomer diffusion through the semicrystalline polymer film surrounding the catalyst crystallite. Diffusion through semicrystalline polymer is a complex process; transport properties are dependent on crystallinity, extent of penetrant sorption and polymer morphology.[23] Since the morphology of the polymer during formation is uncertain, estimation of $(D_i)_s$ is even more difficult. Floyd et al.[5-6] estimate $(D_i)_s$ values for ethylene and propylene in crystalline polyolefins. With values between 10^{-6} and 10^{-8} cm^2/s, it is shown that microparticle diffusion resistance is important only for catalysts of high activity with very large fragment size ($> 0.5\,\mu$). However, in order better to represent catalyst performance under a range of operating conditions and systems, it is desired that $(D_i)_s$ be calculated as a function of operating conditions and system composition.

A correlation suggested by Michaels and Bixler[24] is used to estimate diffusion coefficients in this work. The representation, based on diffusion of vapors through semicrystalline polyethylene, takes into account penetrant molecular size, system temperature, and polymer crystallinity. In the amorphous phase,

the effect of temperature on diffusion is represented through an exponential expression:

$$D_i^* = D_{i_0}^* \exp(-E_{d_i}/RT) \quad (73)$$

Diffusivity is corrected for the presence of crystalline regions according to:

$$(D_i)_s = \frac{D_i^* \alpha_v^n}{\beta_i} \quad (74)$$

where

D_i^* = monomer diffusivity in 100% amorphous polymer,
α_v = volume fraction amorphous phase in polymer, and
β_i = chain immobilization factor for monomer i.

This expression is similar to that for macroparticle diffusion (eq. 14). Diffusivity is corrected both for polymer crystallinity and the reduction of penetrant mobility caused by tightly packed crystallites (β_i). For HDPE, Michaels and Bixler recommend the use of $n = 1.5$ in eq. (74).

Michaels and Bixler relate the parameters in eqs. (73) and (74) to a quantity termed the penetrant reduced molecular diameter (d). The true penetrant molecular diameter (σ) is corrected by a term involving ϕ, the free volume per unit —CH_2— along the polymer chain axis:

$$d = \sigma - \sqrt{\phi}/2 \quad (75)$$

$\sqrt{\phi}/2$ represents the mean unoccupied space between two polymer chain segments; a value of 0.9 Å is used, as suggested in Ref. 24. Values for σ are taken from Reid, Prausnitz, and Sherwood.[25] This reduced diameter is used in the estimation of parameters as follows:

$$\ln\left(\frac{10^7 D^*}{\sigma^2}\right) = 3.66 - 1.32\, d \quad (76)$$

$$\alpha_v \leq 0.8 \quad \ln(\beta) = 0.079\, d^2$$

$$\alpha_v > 0.8 \quad \beta = 1 \quad (77)$$

$$E_d = 2.6 + 2.2\, d \quad (78)$$

Equation (76) gives D^* at 25°C in units of cm^2/s; E_d has units of (kcal/mol K). Equation (77) has been modified so that at high amorphous fractions, it is assumed that crystallites provide negligible impedance to penetrant diffusion.

In Ref. 16, it is shown that the correlation of Michaels and Bixler provides reasonable estimates of $(D_i)_s$ as a function of temperature, penetrant size, and polymer crystallinity. However, it does not consider enhanced diffusivities caused by polymer swelling, nor mixture effects in multicomponent systems. As penetrant concentration increases in the polymer phase, diffusion coefficients can increase significantly.[26-27] Thus, the diffusivities predicted by this correlation are generally at the lower limit of the possible range. It is shown that use of this lower-limit value results in the prediction of negligible diffusion resistance in the microparticle. Thus the use of a more complex correlation is not justified at this time.

EXAMPLE 1: PREDICTION OF PARTICLE MORPHOLOGY

In the previous article of this series,[18] a study of the effects of operating conditions on particle growth and morphology is presented. Some experimental evidence indicates that void fraction decreases throughout polymerization with some catalyst systems. For others, it is necessary to prepolymerize in order to obtain good particle morphology and high bulk density. The multigrain model can be used to simulate growth at similar reaction conditions and a comparison of model results with the experiment provides a useful check on model validity.

The basecase set of simulation parameters are listed in Table III. Rate constants and activation energies for propagation and deactivation reactions have been chosen based on the experimental results presented in Ref. 18. The catalyst diameter (50 μm) was obtained from the supplier; other catalyst parameters are typical for a high activity Mg-supported catalyst.

Effect of Temperature

Rate curves in the temperature range of 40–80°C are presented in Figure 4. A comparison with the experimental instantaneous curves of Ref. 18 indicates that reasonable values have been chosen for the kinetic constants. The shape of the curves is influenced by monomer mass transfer efficiency (Fig. 5a) and the rate of catalyst deactivation (Fig. 5b). The overall monomer mass transfer effectiveness factor across the particle is defined as:

$$\eta_{macro} = \frac{\int_V [M]_{crys}[Me]\, dV}{\eta^* [M]_b \int_V [Me]\, dV} \quad (79)$$

Table III Basecase Simulation Parameters for Example 1: Propylene Polymerization in Heptane Diluent

Kinetic Parameters:	
C_p (potential site frac)	0.2
T_{ref} (K)	328.15
Activation by Alkyl:	
k_a (at T_{ref})	9.43E3
E_a (kcal/mol)	11.0
Propagation:	
k_p (at T_{ref})	9.18E4
E_p (kcal/mol)	10.0
Transfer to Alkyl:	
k_{tr} (at T_{ref})	9.47
E_{tr} (kcal/mol)	14.0
Spontaneous Transfer:	
k_{tr} (at T_{ref})	1.89E-2
E_{tr} (kcal/mol)	14.0
Spontaneous Deactivation:	
k_d (at T_{ref})	8.63E-5
E_d (kcal/mol)	1.0
Polymer Parameters:	
ρ_{pol} (g/cm^3)	0.905
α_v	0.37
C_p (cal/g K)	0.48
$-\Delta H_p$ (kcal/mol)	25.5
Catalyst Parameters:	
d_{cat} (μm)	50.0
τ (tortuosity)	6.0
ϵ_0	0.25
d_{crys} (μm)	0.01
ρ_{cat} (g/cm^3)	2.84
w_{Ti}	0.02
MW_{Ti}	47.90
Operating Conditions:	
P (atm)	7.8
[Al] (mol/L)	1.0E-2
Reaction Time (sec)	5400
Boundary Layer Correlations:	R–M

This ratio provides a measure of effectiveness as weighted by the metal content of the particle. The increase of η_{macro} with time, seen in Figure 5(a), is a result of the dilution effect of the newly formed polymer. As the particle grows in size, its surface area for mass transfer increases and the catalyst concentration seen by the diffusing monomer decreases, leading to a lower monomer volumetric consumption rate.

In Table IV, monomer concentrations, sorption factors (η^*) and diffusion coefficients are tabulated as a function of temperature. Sorption factors and diffusivities increase with increasing temperature.

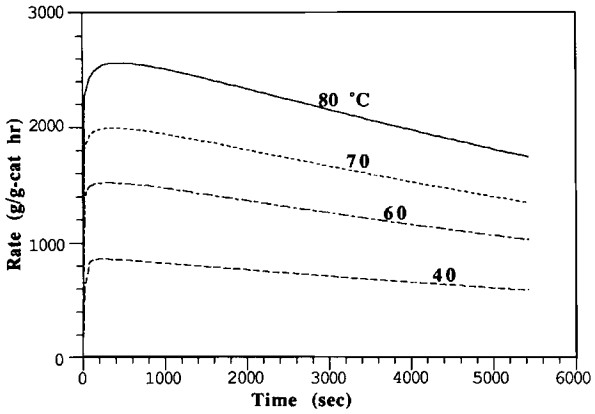

Figure 4 Example 1: Rate curves at 40, 60, 70, and 80°C for propylene polymerization in heptane diluent. Simulation parameters from Table III.

Despite this, the overall effectiveness factor decreases as temperature increases (Fig. 5a). This is due to higher monomer consumption rates at the

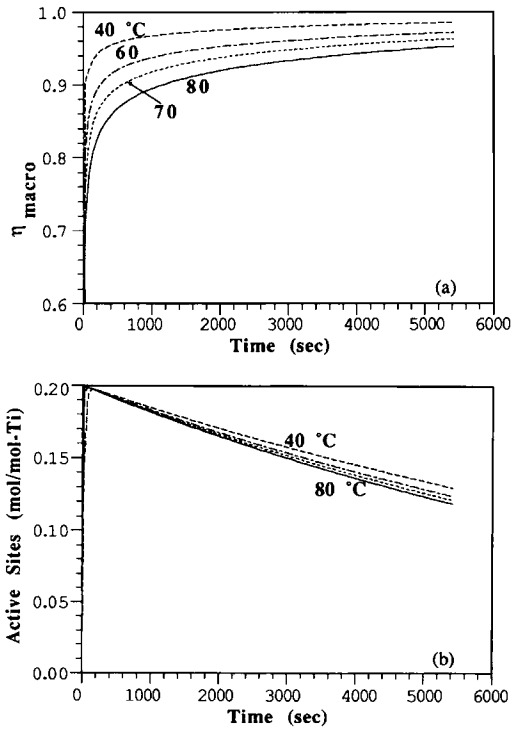

Figure 5 Example 1: Effect of temperature on: (a) Overall macroparticle mass transfer effectiveness factor; (b) Active site fraction.

Table IV Transport Properties as a Function of Temperature: Propylene in Heptane Diluent at P = 7.8 atm

Temperature (°C)	$[M]_b$ (mol/L)	η^*	D_b (cm²/sec)	D_s (cm²/sec)
40	4.20	0.394	8.1E-5	1.0E-7
60	2.60	0.449	9.3E-5	2.9E-7
70	2.12	0.479	10.0E-5	4.7E-7
80	1.75	0.510	10.8E-5	7.4E-7

higher temperatures. All significant mass transfer resistance is at the macroparticle level; mass transfer effectiveness across the microparticles is greater than 0.99 for all simulations.

The local, dimensionless monomer concentration at any point in the macroparticle can be defined as:

$$C_{local} = \frac{[M]_{crys}}{[M]_{particle\ surface}} = \frac{[M]_{crys}}{\eta^* [M]_b} \qquad (80)$$

The quantity C_{local} is a measure of total mass transfer limitations as a function of position in the macroparticle. Figure 6 shows profiles of monomer efficiency as a function of position within the growing macroparticle. The profiles are for the two extremes of the temperature range (40 and 80°C) at reaction times of 30, 300, and 3000 seconds. Although mass transfer limitations decrease quickly with time, significant monomer concentration gradients exist across the particle radius in the early stages of the 80°C reaction. These concentration gradients affect the local rates of polymer production and microparticle growth, as shown by Figure 7. After 30 sec

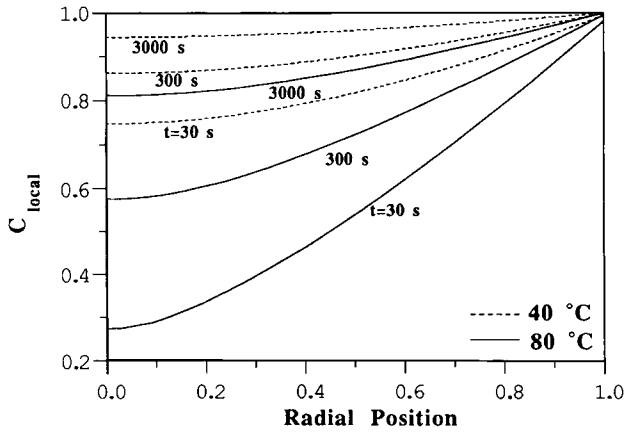

Figure 6 Dimensionless monomer concentration as a function of radial position (Example 1): Profiles at 30, 300, and 3000 sec for reactions at 40 and 80°C.

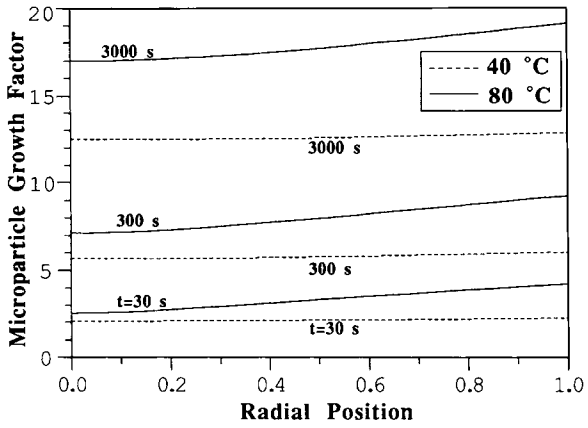

Figure 7 Microparticle growth factors as a function of radial position (Example 1): Profiles at 30, 300, and 3000 sec for reactions at 40 and 80°C.

at 80°C, the microparticles at the center of the particle have a growth factor of only 2.5, while those at the outer edge have grown by a factor 4. At 40°C, where there are negligible concentration gradients, the microparticles grow at almost identical rates across the macroparticle radius.

The predicted effect of reaction conditions on particle void fraction is shown in Figure 8(a). The uneven microparticle growth rates at short reaction times lead to variable void fraction across the particle. Faster growth rates at the outer edge of the particle cause separation of microparticle layers and increased voids. However, as the concentration gradients disappear with time, microparticle growth rates become more uniform across the particle; the void fraction decreases back towards the value for the original catalyst. Overall particle void fractions, averaged over particle radius, are shown in Figure 8(b). The results mirror the experimental trends presented in Ref. 18; particle void fraction decreases with increasing reaction time and with decreasing reaction temperature.

Effect of Prepolymerization

The above results indicate that the most severe profiles for monomer concentrations, microparticle growth factors, and void fractions are early in the particle lifetime. Prepolymerization is one means of controlling particle growth during this critical period. The experimental results of Ref. 18 show that prepolymerization results in both better particle morphology (characterized by bulk density) and a slightly higher average production rate. It is possible to use the multigrain particle model to examine the effects of prepolymerization on particle growth.

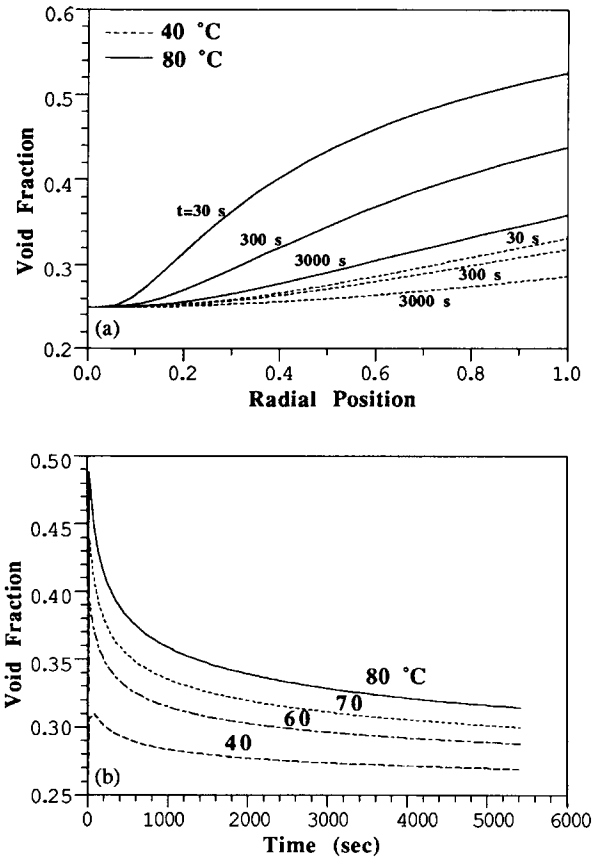

Figure 8 Predicted void fractions for growing polymer particle (Example 1): (a) Radial profiles at 30, 300, and 3000 sec for reactions at 40 and 80°C; (b) Overall void fraction vs. time.

In this set of simulations it is assumed that the prepolymerization step has no effect on the kinetics of the reaction, and that the void fraction of the prepolymerized particle is identical to that of the initial catalyst. The latter assumption is equivalent to assuming that no mass transfer limitations exist during the prepolymerization stage—a valid assumption for the mild operating conditions generally used. The prepolymerization growth factors chosen for the simulations correspond to the prepolymerization yields measured experimentally, as summarized in Table V.

Figure 9(a) compares the macroparticle effectiveness factors at 75°C for a prepolymerized particle ($\phi_0 = 10$) and a particle without prepolymerization. Although the curves meet at long times, there is a significant difference in the monomer concentration gradients in the critical early stages of polymerization, as shown in Figure 9(b). The prepolymerized particle has less severe concentration gradients across its radius due to the presence of the initial polymer.

The effect of prepolymerization on void fraction profiles is shown in Figure 10(a). Without severe concentration profiles, the variation in void fraction across the radius of the prepolymerized particle is small compared to the particle without prepolymerization. Overall macroparticle void fraction as a function of time is shown as Figure 10(b). The prepolymerized particle does not have the initial poor particle morphology shown by the particle which has not undergone a prepolymerization step. However, by the end of the 90 min reaction, the simulation indicates that the void fractions of the two particles are similar.

In parallel with the experimental study,[18] simulations were performed at 60 and 70°C. Table V compares overall void fractions and 90 min average activities for particles with and without prepolymerization at different temperature levels. Experimental values and standard deviations from Ref. 18 are also included. The simulations predict the trends observed experimentally. Prepolymerization leads to a slight increase in observed activity and a decrease in intraparticle void fraction (corresponding to an

Table V Prepolymerization Results: Simulation vs. Experimental. Simulation Parameters from Table III; Experimental Results (± Standard Deviation) from Ref. 18.

Conditions		Experimental Results			Simulation Results		
Temp (°C)	Startup	R_{ob} (g/gcat h)	ρ_{bulk} (g/cm^3)	Prepolym Yield (g)	Initial Growth Factor	Particle Void Fraction	R_{ob} (g/gcat h)
60	Normal	1480 ± 94	0.445 ± 0.012	0	1	0.288	1297
	Prepolym	1527 ± 136	0.457 ± 0.009	182	8	0.282	1304
70	Normal	1593 ± 167	0.416 ± 0.025	0	1	0.300	1705
	Prepolym	1760 ± 186	0.441 ± 0.017	269	9	0.292	1714
75	Normal	1626 ± 68	0.360 ± 0.023	0	1	0.307	1943
	Prepolym	1981 ± 230	0.404 ± 0.018	314	10	0.297	1956

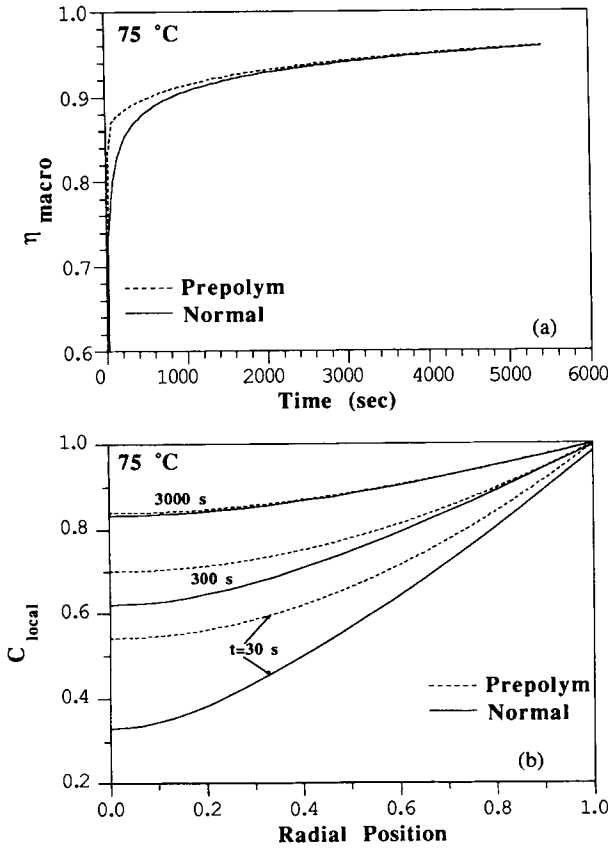

Figure 9 Mass transfer limitations for a prepolymerized particle ($\phi_0 = 10$) and a particle without prepolymerization. Simulation at 75°C, parameters from Table III. (a) Overall effectiveness factor vs. time; (b) Dimensionless monomer concentration radial profiles at 30, 300, and 3000 sec.

increase in bulk density). The relative differences in these quantities increase with increasing reaction temperature. However, the magnitudes of the predicted differences are smaller than those observed experimentally. According to the simulations, the initial advantage of prepolymerization over normal startup (lower void fraction) is lost in the later stages of polymerization as the concentration gradients disappear. Although the model gives the correct trends, it does not provide a perfect match with experimental results.

Experimentally, it is observed that the combination of high temperature and low pressure leads to the formation of poor polymer.[18] The model predicts the same trends. Figure 11 compares results for reactions at 2 and 7.8 atm at 75°C (no prepolymerization). The lower monomer concentration at 2 atm causes slower particle growth; thus the diffusion controlled period lasts longer (Fig. 11a). The greater mass transfer resistance leads to high internal voids within the particle (Fig. 11b). The decreased monomer concentration also results in an increase in the relative ratio of chain transfer to chain growth. Fig. 11c is a plot of M_n (number average MW) for the two cases—at a pressure of 2 atm, M_n is 5 times lower than at 7.8 atm. This lower value corresponds to the high MI values observed at high temperature, low pressure operating conditions, and explains the stickiness of the polymer observed during poor product formation.

Effect of Catalyst Design

It is useful to examine the effects that catalyst parameters, such as particle size and initial void fraction, have on the dynamic process of particle growth. Figure 12 shows overall reaction rates, monomer efficiencies and void fractions for catalyst particles of varying size with initial void fraction of 0.25. The

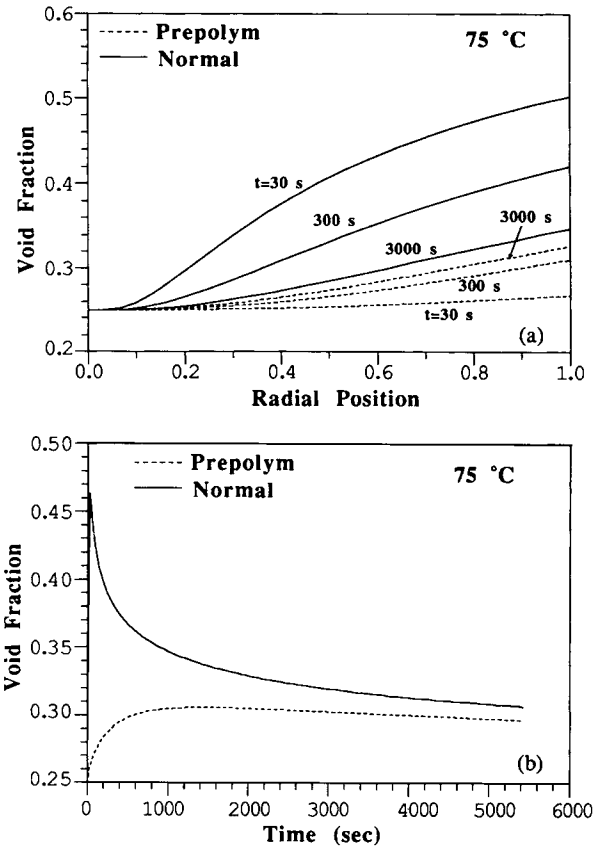

Figure 10 Void fractions for a prepolymerized particle ($\phi_0 = 10$) and a particle without prepolymerization. Simulation at 75°C, parameters from Table III. (a) Radial profiles at 30, 300, and 3000 sec; (b) Overall void fraction vs. time.

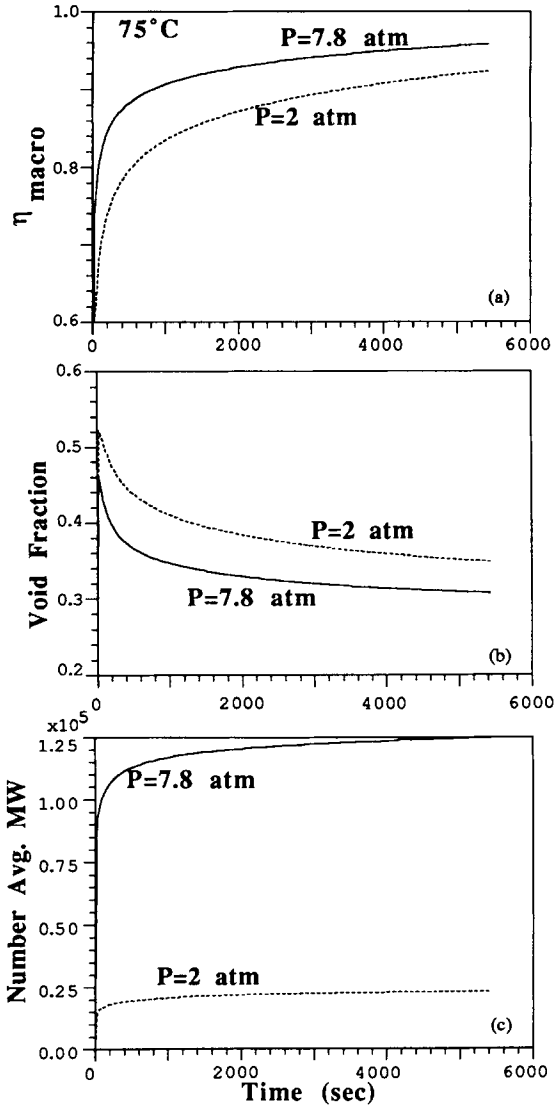

Figure 11 A comparison of polymerization performance at 75°C for reactions at 7.8 and 2.0 atm (simulation parameters as in Table III): (a) Macroparticle effectiveness factor; (b) Particle void fraction; (c) Number average MW.

simulations are at 75°C, with other parameters kept at the basecase values of Table III. As predicted by the macroparticle mass balance (eq. 5), increasing catalyst size has a dramatic effect on mass transfer limitations. The increased catalyst volume results in a large increase in monomer consumption rate relative to the rate of diffusion, creating severe concentration profiles that persist with time (Fig. 12b). These mass transfer limitations lead to a lower production rate (Fig. 12a) and increased intraparticle void fraction (Fig. 12c). With the larger particles, the high predicted void fractions may even lead to particle disintegration.

The effects of initial catalyst void fraction on polymerization rate and particle morphology are less severe, as shown in Figure 13. The simulations are for a catalyst particle with a diameter of 50 μm. As the catalyst void fraction is decreased, the value of the macroparticle diffusivity coefficient decreases, causing the reaction to become more mass transfer limited (Figs. 13a,b). Predicted particle void fractions during polymerization are shown in Figure 13(c). Although the catalyst with $\epsilon_0 = 0.2$ has the

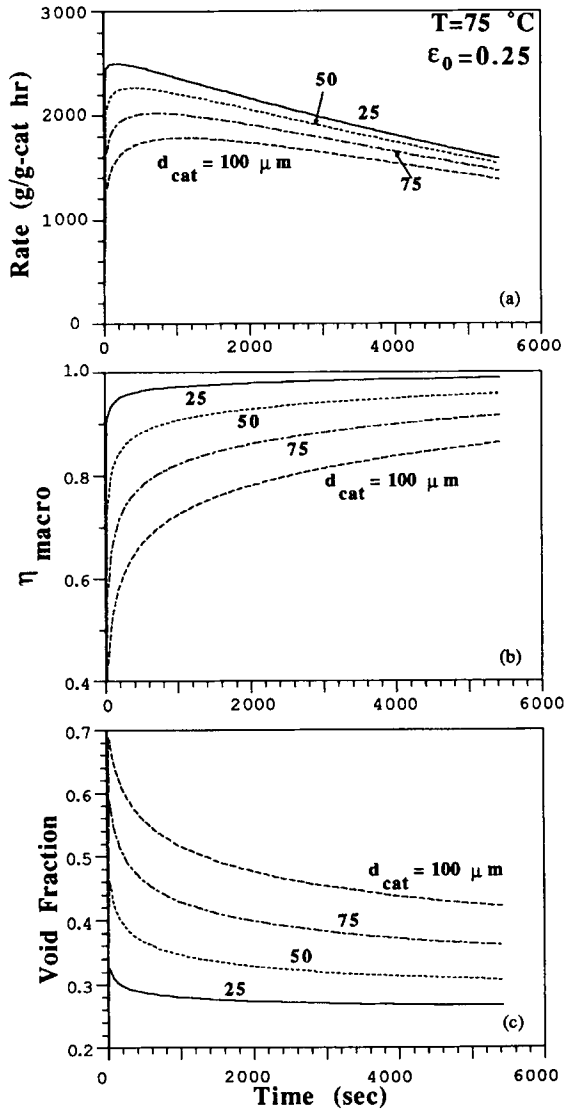

Figure 12 Effect of catalyst diameter on particle growth at 75°C (simulation parameters as in Table III): (a) Observed polymerization rate; (b) Macroparticle effectiveness factor; (c) Particle void fraction.

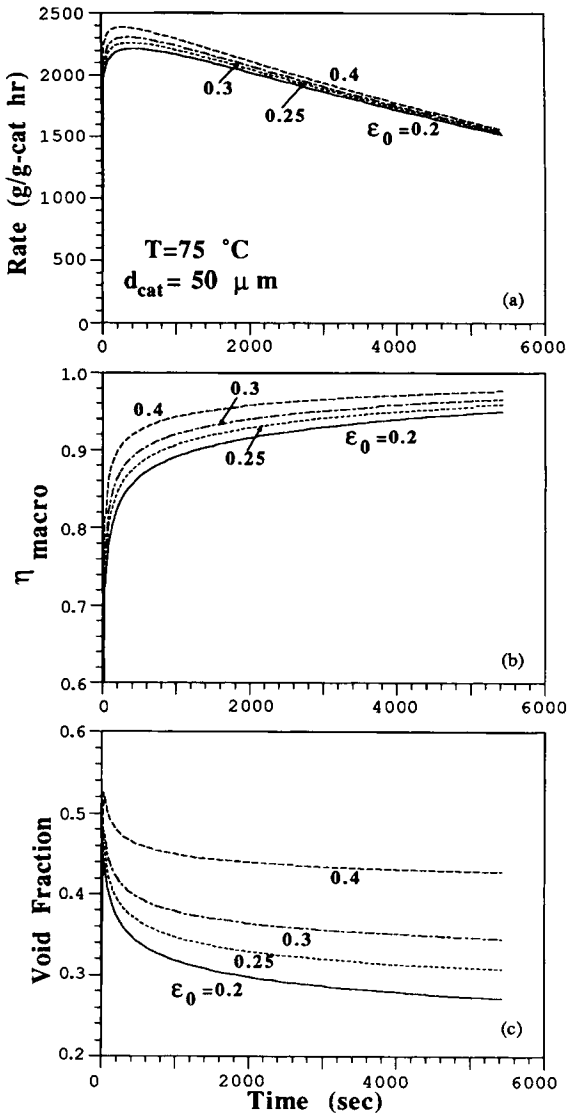

Figure 13 Effect of initial catalyst void fraction on particle growth at 75°C (simulation parameters as in Table III): (a) Observed polymerization rate; (b) Macroparticle effectiveness factor; (c) Particle void fraction.

lowest final void fraction, it shows the largest increase relative to the initial value. This is because of the more severe mass transfer limitations for the low porosity particle. The model predicts, however, that particle morphology is more strongly affected by initial catalyst diameter than by initial catalyst void fraction.

It is also interesting to examine the effect that poor catalyst preparation has on particle growth and morphology. Some catalysts are prepared by contacting the substrate (e.g., silica) with the active metal component in liquid form (e.g., $TiCl_4$). With

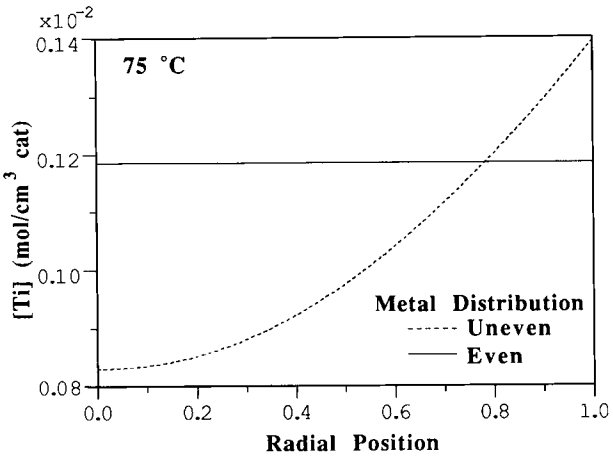

Figure 14 Metal profile specified across catalyst radius—even (w_{Ti} = 0.02) vs. uneven (w_{Ti} = 0.014 + 0.010 r^2) distributions.

insufficient contacting time or low substrate porosity, it is possible to end up with a nonuniform distribution of active metal across the radius of the catalyst particles. Figure 14 shows an example where the metal concentration at the center of the particle is just over half that at the outer edge of the particle; in terms of weight fraction metal, the profile is given by:

$$w_{Ti} = 0.014 + 0.010r^2;\ 0 \le r \le 1 \qquad (81)$$

The overall average metal fraction across the particle is equal to the basecase value of 0.02, shown by the flat profile in Figure 14.

The effect of uneven metal distribution is disastrous. As shown by Figure 15, the predicted void

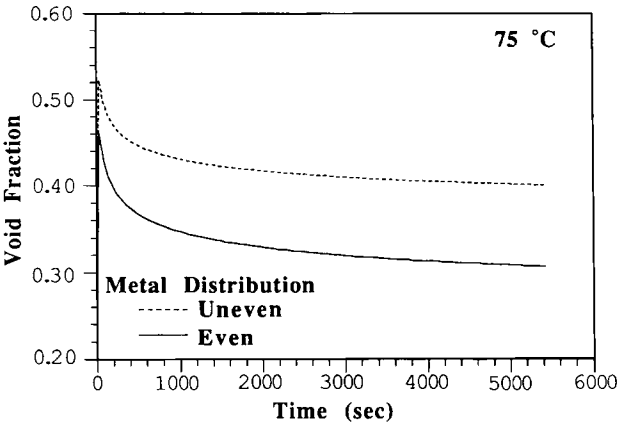

Figure 15 Effect of uneven metal profile on intraparticle void fraction. Reaction at 75°C, other simulation parameters as in Table III.

fraction within the particle reaches a level of greater than 0.5, decreasing very little with time. The uneven metal distribution causes uneven microparticle growth rates within the particle, which persist throughout the reaction. This can be contrasted to the case where uneven microparticle growth rates are caused by concentration profiles; for that situation, the profiles quickly flatten out. This is illustrated by Figure 16, which shows growth factors as a function of particle radius at 30, 300, and 3000 sec.

The simulations in this section show the importance of good catalyst design. Of special importance is the distribution of active metal within the catalyst particle. Any type of uneven distribution leads to uneven particle growth throughout the reaction. In the extreme situation, this can lead to the formation of hollow particles or particle fragmentation. Catalyst particle size and initial porosity are also important design parameters for controlling particle morphology.

EXAMPLE 2: LLDPE PRODUCTION–GAS VS. SLURRY

In previous articles,[4–7,18,21,28] the problem of comparing catalyst performance in gas and slurry reactors has been touched upon. The external boundary layer analysis of Ref. 28 explains the relative tendencies of particles in gas and liquid phase reactors to overheat. In Ref. 21, it is shown that sorption effects in the two reactors are quite different, and must be understood in order to reconcile the observed differences in intrinsic activity. With the full multigrain model, it is possible to combine the previous analyses with the consideration of intraparticle diffusion limitations. The example in this section compares gas and liquid phase polymerization behavior for a catalyst used for the production of LLDPE with butene comonomer.

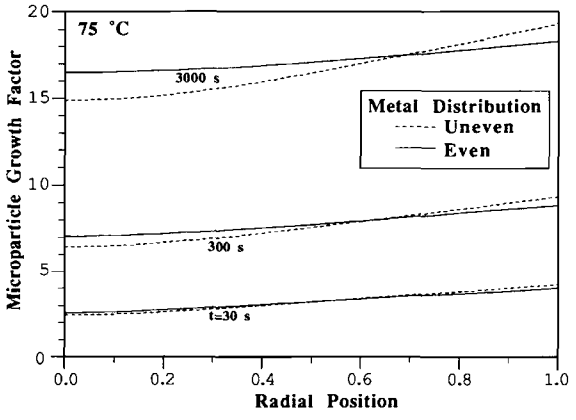

Figure 16 Effect of uneven metal profile: Microparticle growth factors as a function of radial position. Radial profiles at 30, 300, and 3000 sec for reaction at 75°C.

The simulation conditions are summarized in Table VI. The simulation is for a high activity Mg-supported Ti catalyst with initial void fraction of 0.3 and diameter 60 μm. Ranz-Marshall correlations are used to estimate boundary layer heat and mass transfer coefficients, as presented in Ref. 28. A simple kinetic scheme is used in order to concentrate on the physical aspects of particle growth. A reactivity ratio for ethylene to butene propagation of 30 has been assumed. Polymer density is represented as a function of composition according to:

$$\rho_{pol} = 0.9600 - 1.0\phi_{but} + 5.0\phi_{but}^{2} \qquad (82)$$

This fits the composition–density data of Echevskaya et al.[29] for LLDPE consisting of less than 0.10 mole fraction butene.

Although simulation conditions are identical in most regards for the two cases (gas and slurry), there is one major difference. The liquid phase simulation is run with equal mole fractions of butene and ethylene, while for the gas phase simulation, ethylene reactor concentration is set to five times that of butene (see Table VII). Because of the enhanced gas phase sorption of the butene monomer relative to ethylene, its concentration must be kept lower in the reactor to obtain polymer of the desired composition.

Table VII provides a summary of estimates for the diffusion and sorption coefficients in the two reactor environments. Some differences are immediately apparent. Ethylene monomer concentration is higher in the liquid phase by over a factor of two; this suggests that the observed rate of polymerization should be about double that of the gas phase reaction. However, monomer diffusivities in the liquid are much lower—the reaction in the slurry phase is more prone to macroparticle diffusion limitations in the growing polymer particle. Sorption effects play a major role in the gas phase—the relative concentration of butene to ethylene changes by a factor of seven as the monomers are sorbed from the gas phase environment into the polymer. Microparticle diffusivity values, as calculated by eq. (74), are dependent upon polymer crystallinity. For polymer consisting of 4.5 mol % butene, polymer density and volume fraction amorphous are estimated at 0.925 g/cm^3 (by eq. 82) and 0.5, respectively.

Table VI Simulation Parameters for Example 2: LLDPE Production in Gas Phase and Hexane Slurry (1 = Ethylene, 2 = Butene)

Kinetic Parameters:	
C_p (potential site frac)	0.25
T_{ref} (K)	353.15
Activation by Alkyl:	
k_a (at T_{ref})	1.01E4
E_a (kcal/mol)	8.0
Propagation:	
E_p (kcal/mol)	7.0
$k_{p_{11}}$ (at T_{ref})	2.09 E6
$k_{p_{12}}$ (at T_{ref})	6.98E4
$k_{p_{21}}$ (at T_{ref})	2.09E5
$k_{p_{22}}$ (at T_{ref})	2.79E4
Spontaneous Deactivation:	
k_d (at T_{ref})	1.20E-4
E_d (kcal/mol)	1.0
Operating Conditions:	
T (°C)	80.0
P (atm)	35.0
[Al] (mol/L)	1.0E-2
Reaction time (sec)	10000
Gas Velocity (cm^2/sec)	50.0
Boundary Layer Correlations:	R–M
Polymer Parameters:	
$(\rho_{p_{cr}})_1$ (g/cm^3)	0.997
$(\rho_{p_{cr}})_2$ (g/cm^3)	0.91
$(\rho_{p_{am}})_1$ (g/cm^3)	0.854
$(\rho_{p_{am}})_2$ (g/cm^3)	0.85
$-\Delta H_p$ (kcal/mol)	25.5
C_p (cal/g K)	0.48
Catalyst Parameters:	
d_{cat} (μm)	60.0
τ (tortuosity)	4.0
ϵ_0	0.30
d_{crys} (μm)	0.01
ρ_{cat} (g/cm^3)	2.84
w_{Ti}	0.02
MW_{Ti}	47.90

Figures 17 and 18 show the predicted behavior of the catalyst system in gas phase and slurry reactors. The polymer production rate is higher in the slurry phase (Fig. 17). Note, however, that it is not double the gas phase rate, as would be expected from the bulk monomer concentrations. The shape of the rate curves differ slightly for the two systems early in the reaction, although both show the long term deactivation representative of these systems. Polymer composition (Fig. 18) remains constant throughout the gas phase reaction, but shows a slow drift with time for the slurry system. Despite the large difference in monomer concentration ratios between the gas phase and liquid systems, the resulting polymers are roughly the same composition; this again illustrates the importance of monomer sorption effects.

Macroparticle effectiveness factors for ethylene and butene are shown in Figure 19. The liquid phase reaction is severely mass transfer limited throughout

Table VII Transport Properties for LLDPE Production at 80°C: Gas Phase vs. Hexane Slurry

	$[M]_b$ (mol/L)	η^*	D_b (cm^2/sec)	D_s (cm^2/sec)
Gas Phase (in N_2):				
Eth (x = 0.5)	0.652	0.55	5.7E-3	1.8E-6
But (x = 0.1)	0.130	3.75	2.8E-3	7.7E-7
Liquid (in Hexane):				
Eth (x = 0.2)	1.365	0.47	1.5E-4	1.6E-6
But (x = 0.2)	1.365	0.47	9.8E-5	6.5E-7

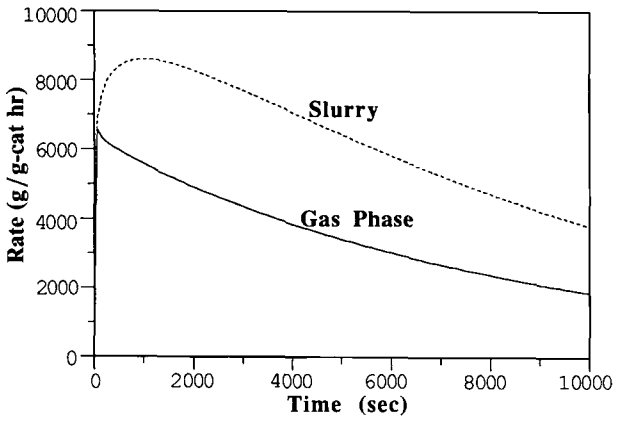

Figure 17 Example 2: LLDPE production rates at 80°C in gas phase and hexane slurry reactors. Simulation parameters from Tables VI and VII.

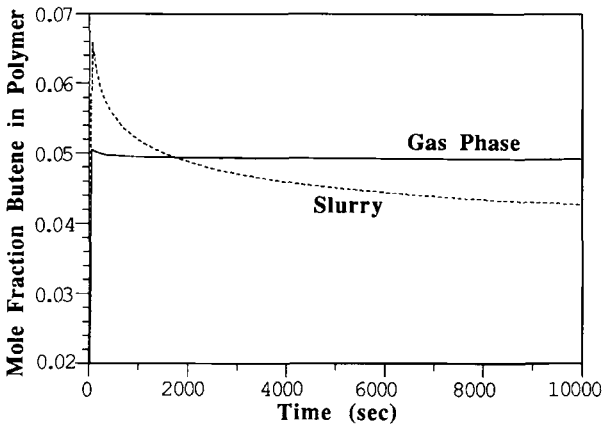

Figure 18 Observed copolymer composition for Example 2: butene mol fraction vs. time.

much of the reaction, while the gas phase system has negligible mass transfer resistance. The mass transfer resistances for the slurry reaction are the cause of the observed differences in the rate curve shapes seen in Figure 17. Figure 20 shows dimensionless monomer concentration profiles across the particle at different times throughout the reaction. Thirty minutes into the reaction, the ethylene concentration at the center of the particle in the slurry phase is only 0.4. However, the same catalyst system shows negligible mass transfer resistance in the gas phase environment. Note that even though diffusion coefficients are smaller for butene, ethylene is more mass transfer limited because of its higher rate of consumption.

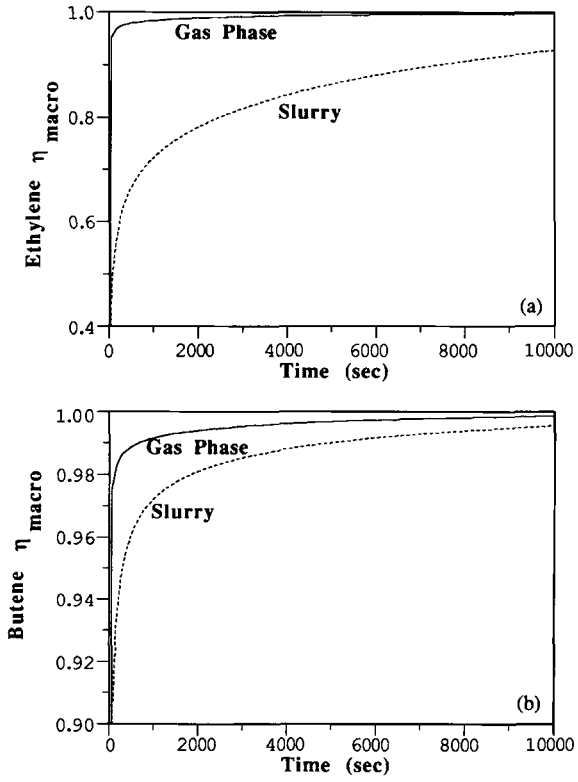

Figure 19 Overall macroparticle effectiveness factors for Example 2: (a) ethylene; (b) butene.

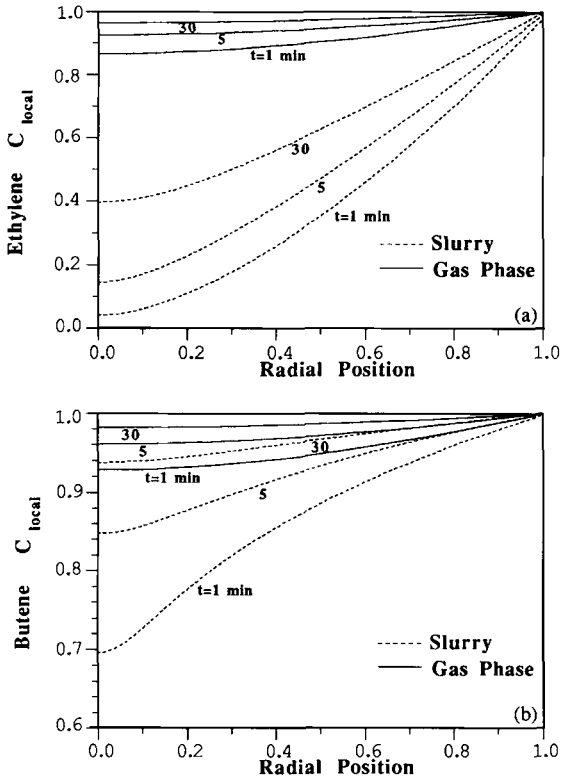

Figure 20 Dimensionless monomer concentrations as a function of radial position for Example 2. Profiles at 1, 5, and 30 min for: (a) ethylene; (b) butene.

The mass transfer limitations observed in the slurry phase lead to heterogeneity in polymer composition across the particle. Copolymer composition is shown as a function of radius in Figure 21. Because the slurry phase particle is ethylene starved at the center, particularly early in the polymerization, the polymer formed has a very high butene content. This can be contrasted to the gas phase polymerization, for which composition remains uniform across the particle. Although the polymer at the center of the particle in the slurry phase has a high butene fraction, very little polymer is formed because of the much lower butene reactivity. This can be seen by examining Figure 22; microparticles at the center of the slurry phase particle are significantly smaller in size than those at the outer edge.

Due to the lower production rate of butene rich polymer, overall polymer composition for the slurry

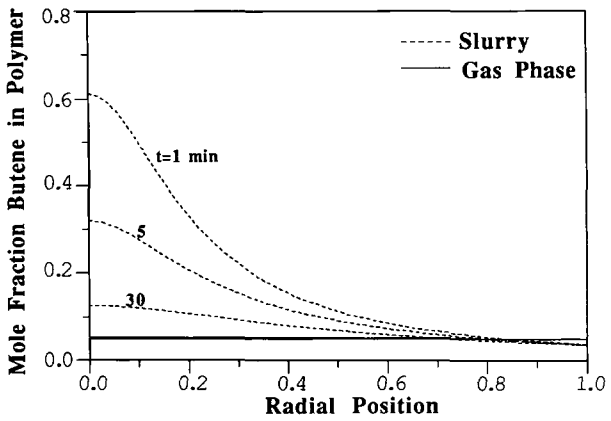

Figure 21 Copolymer composition as a function of radial position for Example 2. Profiles at 1, 5, and 30 min.

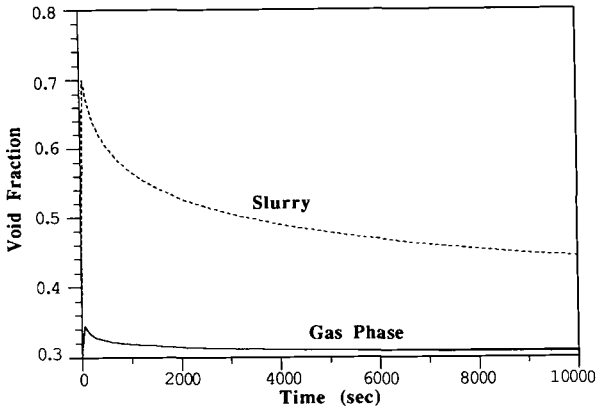

Figure 23 Macroparticle void fraction vs. time for Example 2.

phase reaction does not drift over time as much as might be expected from the changing concentration profiles (see Fig. 18). However, the uneven growth rates across the particle leads to very poor morphology for the slurry phase particle. Figure 23 indicates that the void fraction reaches as high as 0.7 early in the reaction, and is still at a level of 0.5 at the end of the reaction. This can be contrasted to the gas phase particle, for which the void fraction remains close to its initial value of 0.3.

This example illustrates the difficulties in predicting catalyst performance in the gas phase based on slurry phase results or vice versa. The differences in the physical systems strongly affect monomer sorption and diffusion behavior. This can create a situation in which catalyst performance is kinetically controlled in the gas phase, but is severely mass transfer limited in the slurry reactor. The mass transfer limitations, in turn, affect not only the observed rate curve, but also polymer composition and particle morphology. The multigrain particle model is a valuable tool for examining the importance of diffusion limitations on polymerization behavior for a complete range of operating conditions and systems.

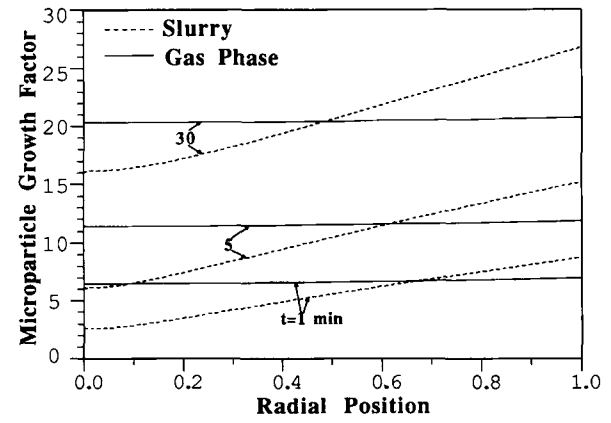

Figure 22 Microparticle growth factors as a function of radial position for Example 2. Profiles at 1, 5, and 30 min.

SUMMARY

Significant extensions have been made to the multigrain particle model. These changes include:

- An improved numerical solution technique;
- Extension to multiple monomer systems;
- The introduction of correlations for diffusion coefficients and sorption factors as a function of operating system and conditions;
- Specification of active metal concentration as a function of radius;
- The estimation of reactor monomer concentrations and fluid properties as a function of operating conditions and composition;
- Prediction of particle void fraction as a function of radius;
- The addition of a comprehensive copolymerization kinetic scheme.

The examples illustrate the usefulness of the multigrain particle model in addressing many interesting questions in the area of heterogeneous catalyzed olefin polymerization. By including correlations to calculate fluid properties, monomer diffusivities and sorption factors as a function of

operating conditions, fluid composition, and phase, it is possible to predict catalyst performance under a wide range of conditions using a single set of kinetic parameters. The model also gives some insight on the effect of uneven growth on particle morphology, and the role that prepolymerization plays in controlling morphology. A future article will deal with the topic of copolymerization in more detail.

REFERENCES

1. W. H. Ray, *Transition Metal Catalyzed Polymerizations*, R. P. Quirk, Ed., Cambridge University Press, New York, 1988, p. 563.
2. B. E. Wagner and F. J. Karol, Paper presented at SPE RETEC Meeting, Houston, TX, 1989.
3. M. Kakugo, H. Sadatoshi, J. Sakai, and M. Yokoyama, *Macromolecules*, **22**, 3172 (1989).
4. S. Floyd, K.-Y. Choi, T. W. Taylor, and W. H. Ray, *J. Appl. Polym. Sci.*, **32**, 2231 (1986).
5. S. Floyd, K.-Y. Choi, T. W. Taylor, and W. H. Ray, *J. Appl. Polym. Sci.*, **32**, 2935 (1986).
6. S. Floyd, Ph. D. Thesis, University of Wisconsin–Madison, 1986.
7. S. Floyd, T. Heiskanen, T. W. Taylor, G. E. Mann, and W. H. Ray, *J. Appl. Polym. Sci.*, **33**, 1021 (1987).
8. J. W. Begley, *J. Polym. Sci. A-1*, **4**, 319 (1966).
9. D. Singh and R. P. Merrill, *Macromolecules*, **4**, 599 (1971).
10. W. R. Schmeal and J. R. Street, *J. Polym. Sci. Polym. Phys. Ed.*, **10**, 2173 (1972).
11. E. J. Nagel, V. A. Kirillov, and W. H. Ray, *I. & E. C. Prod. Res. Dev.*, **19**, 372 (1980).
12. R. L. Laurence and M. G. Chiovetta, *Polymer Reaction Engineering: Influence of Reaction Engineering on Polymer Properties*, K. H. Reichert and W. Geiseler, Eds., Hanser, Munich, 1983, p. 73.
13. M. A. Ferrero and M. G. Chiovetta, *Polym. Eng. & Sci.*, **27**, 1436 (1987).
14. M. A. Ferrero and M. G. Chiovetta, *Polym. Eng. & Sci.*, **27**, 1448 (1987).
15. L. L. Böhm, R. Franke, and G. Thum, *Transition Metals and Organometallics as Catalysts for Olefin Polymerization*, W. Kaminsky and H. Sinn, Eds., Springer-Verlag, Berlin, 1988, p. 391.
16. R. A. Hutchinson, Ph. D. Thesis, University of Wisconsin–Madison, 1990.
17. L. R. Petzold, *DASSL, A Differential/Algebraic System Solver*, SAND82-8637 (1982).
18. R. A. Hutchinson and W. H. Ray, *J. Appl. Polym. Sci.*, to appear (1992).
19. C. M. Chen, Ph. D. Thesis, University of Wisconsin–Madison, 1991.
20. C. N. Satterfield, *Heterogeneous Catalysis in Practice*, McGraw-Hill, New York, 1980, p. 336.
21. R. A. Hutchinson and W. H. Ray, *J. Appl. Polym. Sci.*, **41**, 51 (1990).
22. S. A. Stern, J. T. Mullhaupt, and P. J. Gareis, *AIChE J.*, **15**, 64 (1969).
23. A. Peterlin, *J. Macromol. Sci. Phys.*, **B11**, 57 (1975).
24. A. S. Michaels and H. J. Bixler, *J. Polym. Sci.*, **50**, 413 (1961).
25. R. C. Reid, J. M. Prausnitz, and T. K. Sherwood, *The Properties of Gases and Liquids, 3rd Ed.*, McGraw-Hill, New York, 1977.
26. M. Fels and R. Y. M. Huang, *J. Appl. Polym. Sci.*, **14**, 537 (1970).
27. A. Kreituss and H. L. Frisch, *J. Polym. Sci. Polym. Phys. Ed.*, **19**, 889 (1981).
28. R. A. Hutchinson and W. H. Ray, *J. Appl. Polym. Sci.*, **34**, 657 (1987).
29. L. G. Echevskaya, V. A. Zakharov, and G. D. Bukatov, *React. Kinet. Catal. Lett.*, **34**, 99 (1987).

Received November 20, 1990
Accepted May 14, 1991